PE&RS
August 2024 Volume 90, Number 8
The official journal for imaging and geospatial information science and technology
PHOTOGRAMMETRIC ENGINEERING & REMOTE SENSING

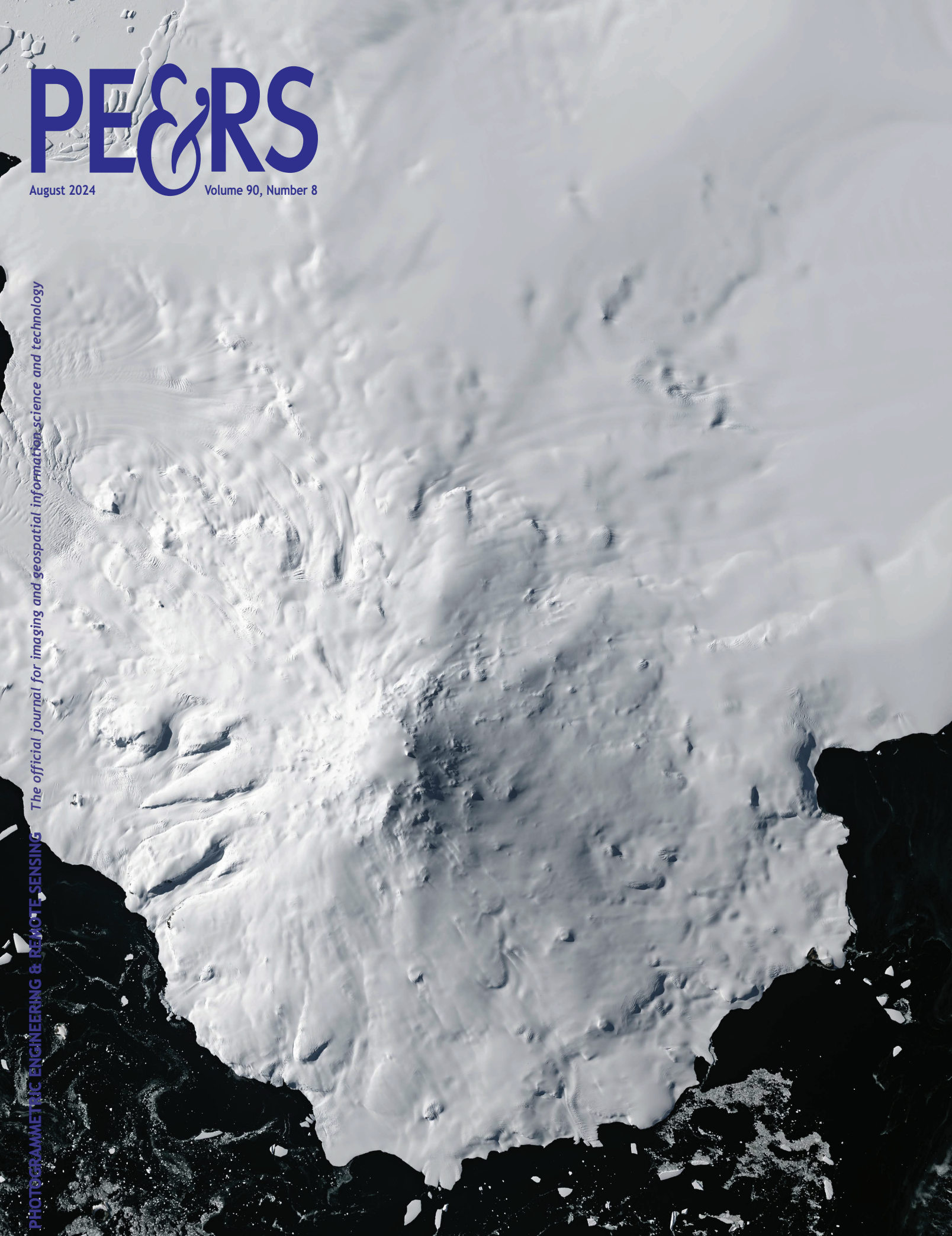

asprs THE IMAGING & GEOSPATIAL INFORMATION SOCIETY

ASPRS MEMBERSHIP

Joining ASPRS is a great way to boost your resume and learn valuable life lessons

WHY GET INVOLVED WITH ASPRS?

- Develop leadership skills
- Experience working on a team
- Gain valuable soft skills
- Network
- Learn about yourself
- Have fun!

Scholarships

The many ASPRS scholarships are only available to student members

Certification

The ASPRS certification program for mapping scientists, photogrammetrists and technologists is the only fully Accredited certification program in the geospatial sciences

Continuing Education

Earn professional development hours and CEUs by attending workshops at our conferences and on-line as well as our monthly on-line geobytes series

PE&RS

Our monthly journal, is packed with informative and timely articles designed to keep you abreast of current developments in your field. Now available in e-format.

Get Connected

facebook.com/ASPRS.org

linkedin.com/company/asprs/about/

twitter.com/ASPRSorg

youtube.com/user/ASPRS

Image and text courtesy the ASPRS Florida Region

asprs FLORIDA REGION THE IMAGING & GEOSPATIAL INFORMATION SOCIETY

ANNOUNCEMENTS

Vexcel 3D Cities, vexceldata.com, is now available with Cesium ion Self-Hosted, bringing high-quality 3D geospatial data for 60+ cities to a global audience. This new collaboration enhances the 3D visualization and analysis capabilities for large metropolitan areas, helping sectors from government to telecommunications, gaming, and more. Explore a new dimension with our 3D mesh models.

Here are highlights from the partnership:

- Global Coverage—Covering over 62,000 km², Vexcel 3D Cities includes major cities at scale in the US, Europe, Australia, and Japan.
- High-Quality Data—Leveraging Vexcel's market-leading photogrammetric UltraCam sensors and extensive aerial imagery library, these models provide an immersive and accurate 3D cityscape.
- Optimized Performance—Using 3D Tiles OGC Community Standard created by Cesium for enhanced streaming and rendering.
- Compatibility—Fully compatible across various platforms like CesiumJS, Cesium for Unreal, Cesium for Unity, and Cesium for Omniverse, promoting flexible integration for various projects.

Learn more and explore some cities in 3D at: https://cesium.com/blog/2024/06/25/vexcel-cesium.

STACK Construction Technologies, an industry-leading cloud-based construction platform, announces a partnership with **Nearmap**, nearmap.com, one of the world's largest location intelligence and aerial imagery solutions providers, to improve efficiency, reduce risks, and increase bid output for subcontractors. The new integration delivers benefits by leveraging high-resolution aerial images to improve estimate accuracy and eliminate the need for onsite visits.

Exterior and site plans on existing buildings are not always available, leaving contractors to use lower-resolution satellite images and increasing safety risks, labor costs, and time wasted by performing redundant onsite visits. With the STACK and Nearmap integration, contractors can seamlessly import high-quality aerial images with automatic scaling to complete quotes. By leveraging STACK›s robust takeoff and estimating tools, contractors will increase bid outputs, have greater scalability, and eliminate risk with a fully remote process.

"The partnership between STACK and Nearmap will deliver valuable impact for contractors," said Phil Ogilby, CEO and Co-Founder of STACK Construction Technologies. "With real-time access to Nearmap premium aerial imagery integrated with STACK's hyper-accurate preconstruction tools, our cloud-based platform empowers subcontractors to not only mitigate safety risks but maximize efficiency."

The integration specifically empowers roofing contractors to deliver precise and detailed estimates on projects like re-roofing, storm damage, and repairs. What used to be a time-consuming task taking hours can now be accomplished in just minutes by reducing the amount of time contractors have to spend onsite. Nearmap imagery enables roofing contractors to view hazards remotely, like building height, landscape features, and powerlines, mitigating safety risks and reducing worker's compensation rates. Estimators can expedite quote generation, ensuring customer satisfaction, while increasing their chances of securing more projects. The utilization of high-quality aerial images enhances the professionalism of the quotes, instilling confidence in project owners and assisting contractors in winning additional contracts.

"We've learned many of our customers want to choose how they access Nearmap imagery and insights within their technology stacks, which includes having the flexibility to access data instantly through the MapBrowser platform, or through a partner like STACK," said Shelly Carroll, General Manager of Geospatial Solutions at Nearmap. "Nearmap is responding to this customer need by adding flexibility and market-leading content including high-resolution 2D aerial imagery and 3D content to better support contractors, enabling our customers to work smarter and more efficiently."

"STACK and Nearmap business models are highly compatible, our commitment to improving customer's business is aligned, and we couldn't be more thrilled about the strength and quick pace at which our partnership has come together," said Ray DeZenzo, COO of STACK Construction Technologies. "We're excited to continue leveraging future Nearmap solutions and innovations as this partnership evolves."

The partnership between STACK and Nearmap marks the beginning of an exciting chapter in construction technology to streamline the preconstruction process. As industry leaders, both organizations are committed to delivering outstanding results, setting new standards for advancement, and accelerating growth for their contractor customers.

NV5, nv5.com, completes Alaska Project with Innovative Multisensor Platform.

Collecting geospatial data in Alaska is not for the faint of heart. The rugged terrain makes it dangerous and expensive to send people out in the field. The extreme weather leaves only limited windows of time to complete aerial surveys. Not to mention the challenges like rapid changes with freezes and thaws impact measurements on the coast, along rivers and over bodies of water.

In prepping for a recent acquisition project to fully characterize the subsurface river bottom in a glacial fed river in South Central Alaska, we knew we would have to address all of these challenges. Because the river was fed by a glacier, the acquisition needed to be done in early spring before the glacial melt introduced silt that would make bathymetric lidar useless in turbid water. The project spanned from coastal mud flats near sea level over heavily braided channels to the glacier feeding the river at an elevation of more

than 4,000 feet. The rapid elevation, combined with rainy and cloudy weather, made it unsafe to do the acquisition via fixed-wing aircraft.

Multisensor Platform on Helicopter Saves Time

Since time was paramount for this project, we devised a plan that enabled our team to do the entire survey during the brief windows when weather cooperated. We used a helicopter equipped with multiple sensors for bathymetric data, lidar, thermal video and oblique photos. So instead of flying a fixed wing aircraft at 1,200 feet, the helicopter allowed us to fly under the clouds and closer to the river to collect better, more accurate data and images. The helicopter also offered greater maneuverability, enabling our crew to pivot and cover all the needed flight lines quickly and efficiently.

Having this multisensor platform affixed to a helicopter enabled us to do the entire acquisition in less than two days. We were able to quickly deploy our team when weather broke, during low tide before the glacial melt started. This approach saved the client time and money, and eliminated the need to send a large crew of ground surveyors to run hundreds of transects in a potentially dangerous river in remote Alaska.

By flying lower and slower with the helicopter, we were able to capture higher density lidar and greater imagery ground sampling distance (GSD), providing a high level of detail to our client. The data collected this spring will be merged into a larger topobathymetric lidar dataset we collected in 2022, which will contribute to a broader watershed analysis.

The **Sanborn Map Company Inc.** (Sanborn), a leader in the geospatial industry, today announced the acquisition of the assets of VeriDaaS, a cutting-edge technology company specializing in Geiger mode lidar. This acquisition aligns with Sanborn's strategic vision to continue growth and provide the latest technology to customers. Sanborn will integrate VeriDaaS assets and innovative solutions into the Mapping Division, enhancing the company's ability to deliver comprehensive and advanced technological solutions and services to customers. This acquisition is expected to drive significant growth in the next few years for the company as the technology has matured significantly since it was first introduced.

"The acquisition of the photon counting lidar technology along with value added product generation is a significant step forward for Sanborn. This groundbreaking technology developed from significant previous investments perfectly complements our commitment to innovation and excellence. We will accelerate our growth in Lidar products and analytics expanding our capabilities to better serve our clients and partners," stated John Copple, CEO of Sanborn.

VeriDaaS developed a significant number of market applications, with a portfolio that includes asset management, vegetation management, solar sighting, flood risk and resilience, wildfire management, urban change analysis and many other applications. The integration of this technology with Sanborn's linear mode Lidar is expected to enhance Sanborn's offerings and provide customers with superior services.

Sanborn was advised by The Environmental Financial Consulting Group, LLC (EFCG) Financial and terms of the transaction were not disclosed.

For more information about the acquisition and what it means for customers and partners please visit https://sanborn.com/ or please contact Mr. Jason Caldwell, Vice President, Business Development, via phone: 719-264-5547, fax: 719-528-5093, email: jcaldwell@sanborn.com.

The Texas Department of Transportation has selected **Woolpert**, woolpert.com, to provide land surveying services under a $3 million, indefinite delivery, indefinite quantity (IDIQ) contract supporting the Houston District.

Under this contract, Woolpert will provide right-of-way maps, design and construction surveys, aerial mapping, horizontal and vertical control, and state land surveying services on an as-needed basis to support a range of highway improvement and maintenance projects throughout the Houston area.

Woolpert Survey Team Leader Thomas Cargill said that these projects will help improve roadway conditions and overall safety for drivers. Cargill, a registered professional land surveyor with 27 years of experience in the surveying profession and 17 years as a TxDOT consultant, joined Woolpert's survey team this year.

"The Houston District has a population of more than 7 million, and its infrastructure supports more than 100 million vehicle miles each day," Cargill said. "We know that safety is the department and the district's No. 1 priority, and we are thrilled to provide the expansive surveying services needed to support their great work."

CALENDAR

- 18-22 August, **SPIE 2024**, San Diego, California; https://spie.org/OP.
- 26 September, **37th Annual GIS in the Rockies**, Denver, Colorado; http://gisintherockies.org/.
- 7-10 October, **GIS-Pro 2024**, Portland, Maine; https://urisa.org/page/GIS-Pro2024.
- 21-25 October, **ASPRS International Technical Symposium**, virtual; https://my.asprs.org/2024symposium.
- 18-22, November, **URISA GIS Leadership Academy**, Fort Worth, Texas; https://urisa.org/page/URISA_AdvancedGLA.
- 2-6, December, **URISA GIS Leadership Academy**, virtual; https://urisa.org/page/URISA_AdvancedGLA.

PE&RS
PHOTOGRAMMETRIC ENGINEERING & REMOTE SENSING
The official journal for imaging and geospatial information science and technology
August 2024 Volume 90 Number 8

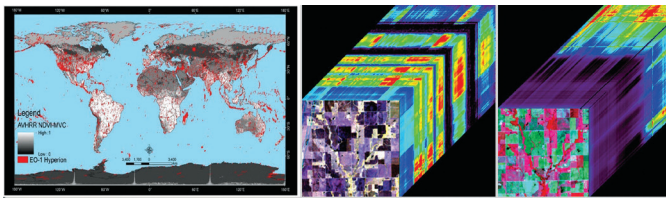

COLUMNS

ANNOUNCEMENTS

DEPARTMENTS

See the Cover Description on Page 456

COVER DESCRIPTION

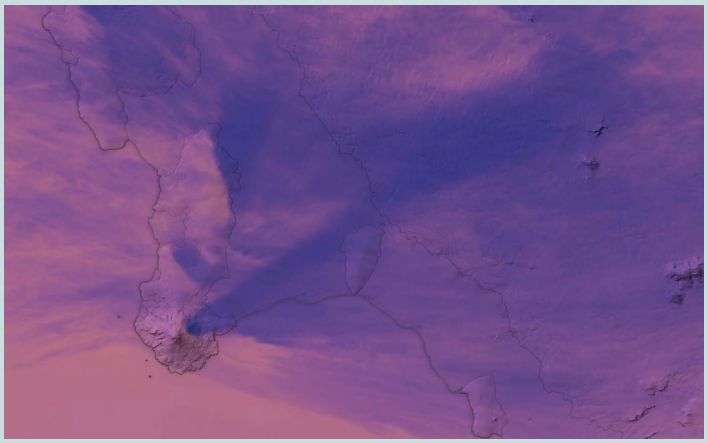

Huge, thick ice sheets blanket much of the Antarctic continent. Amid all this ice, numerous volcanoes dot the landscape. Many are partially buried, with only their tops exposed above the ice sheet's surface—that is, except for Mount Siple. This stately island volcano stands in full view, from sea level to its summit elevation of more than 3,100 meters (10,000 feet).

The OLI-2 (Operational Land Imager-2) on Landsat 9 captured the image of Mount Siple, cover, on February 26, 2024. Sunlight reflects from the snowy, icy surfaces, including the Getz Ice Shelf, which separates the volcano from mainland West Antarctica.

Mount Siple and other Antarctic volcanoes are located in a remote, extreme environment, making them a challenge for scientists to study and monitor. However, remote sensing can help. During the dark winter months, satellite sensors cannot collect the light needed for natural-color images like the cover image, but there are other ways to "see" in the dark.

This false-color image, above, was acquired by the VIIRS (Visible Infrared Imaging Radiometer Suite) on the Suomi NPP satellite. It shows a wider view of Mount Siple and mainland Antarctica on June 9, 2024, during the Antarctic winter. The image was overlaid on data from the Reference Elevation Model of Antarctica (REMA) to give a sense of the topography.

The colors in this image represent brightness temperature, which is useful for distinguishing the relative warmth (orange and pink) or coolness (purple and blue) of various features. Here, clouds appear cooler than the underlying icy surfaces.

Notice the plume streaming inland from near the summit of Mount Siple. The shape of the feature and its relative coolness compared to its surroundings resemble those of a volcanic plume. But according to Simon Carn, a volcanologist at Michigan Tech, it is more likely an orographic cloud. This cloud type forms when the shape of the landscape forces moist air up to altitudes where the water vapor cools and condenses. Carn notes that other satellite data show no indication of sulfur dioxide or ash in the plume. Nor is there a heat signal that would indicate hot volcanic material at or near the summit.

"The absence of all these features, and also the fact that similar features are often seen downwind of other non-volcanic topographic prominences in the Antarctic and Arctic, indicates that the plume is most likely orographically generated," Carn said. "This is also consistent with the plume being 'detached' from (slightly downwind of) the volcano summit."

Speculation about volcanic activity at Mount Siple has occurred in the past, including observations of a possible volcanic plume in 1988. That plume was later determined to be the result of atmospheric effects, according to a report from the Smithsonian Institution's Global Volcanism Program. Researchers noted in a 2021 publication that limited observations have prevented detailed interpretations of Mount Siple's volcanic history, writing: "At this stage, there is no indication that Mount Siple should be considered 'active'."

NASA Earth Observatory images by Michala Garrison, using VIIRS data from NASA EOSDIS LANCE, GIBS/Worldview, and the Suomi National Polar-orbiting Partnership, Reference Elevation Model of Antarctica (REMA) data from the Polar Geospatial Center at the University of Minnesota, and Landsat data from the U.S. Geological Survey. Story by Kathryn Hansen.

Both images can be viewed online by visiting the Landsat Image Gallery, https://landsat.gsfc.nasa.gov/, image id 152988.

asprs
THE IMAGING & GEOSPATIAL INFORMATION SOCIETY

PHOTOGRAMMETRIC ENGINEERING & REMOTE SENSING

Journal Staff

Publisher ASPRS
Editor-In-Chief Alper Yilmaz
Director of Publications Rae Kelley
Electronic Publications Manager/Graphic Artist
Matthew Austin

Photogrammetric Engineering & Remote Sensing is the official journal of the American Society for Photogrammetry and Remote Sensing. It is devoted to the exchange of ideas and information about the applications of photogrammetry, remote sensing, and geographic information systems. The technical activities of the Society are conducted through the following Technical Divisions: Geographic Information Systems, Photogrammetric Applications, Lidar, Primary Data Acquisition, Professional Practice, Remote Sensing Applications, and Unmanned Autonomous Systems. Additional information on the functioning of the Technical Divisions and the Society can be found in the Yearbook issue of *PE&RS*.

All written correspondence should be directed to the American Society for Photogrammetry and Remote Sensing, PO Box 14713, Baton Rouge, LA 70898, including general inquiries, memberships, subscriptions, business and editorial matters, changes in address, manuscripts for publication, advertising, back issues, and publications. The telephone number of the Society Headquarters is 225-408-4747; the fax number is 225-408-4422; web address is www.asprs.org.

PE&RS. *PE&RS* (ISSN0099-1112) is published monthly by the American Society for Photogrammetry and Remote Sensing, 8550 United Plaza Blvd, Suite 1001, Baton Rouge, Louisiana 70809 . Periodicals postage paid at Bethesda, Maryland and at additional mailing offices.

SUBSCRIPTION. *PE&RS* is available as an e-Subscription (single-site and multi-site licenses) and an e-Subscription with print add-on (single-site license only). PE&RS subscriptions are on a calendar-year, beginning in January and ending in December.

The rate for a single-site e-Subscription for the USA/Non-USA is $1040 USD, for Canadian* is $1092 USD.

The rate for a multi-site e-Subscription for the USA/Non-USA is $1040 USD plus $250 USD for each additional license, for Canadian* is $1092 USD plus $263 for each additional license.

The rate for e-Subscription with print add-on for the USA is $1546 USD, for Canadian* is $1637 USD, and for Non-USA is $1596 USD.

*Note: Subscription prices for Canada includes 5% of the total amount for Canada's Goods and Services Tax (GST #135123065). **PLEASE NOTE: All Subscription Agencies receive a 20.00 USD discount.**

POSTMASTER. Send address changes to PE&RS, ASPRS, PO Box 14713, Baton Rouge, LA 70898. CDN CPM #(40020812).

MEMBERSHIP. Membership is open to any person actively engaged in the practice of photogrammetry, photointerpretation, remote sensing and geographic information systems; or who by means of education or profession is interested in the application or development of these arts and sciences. Membership is for one year, with renewal based on the anniversary date of the month joined. Membership Dues include a 12-month electronic subscription to *PE&RS*. Annual Individual Membership dues are $175.00 USD and Student Membership dues are $50.00 USD. A tax of 5% for Canada's Goods and Service Tax (GST #135123065) is applied to all members residing in Canada.

GIS Tips & Tricks

By Al Karlin, Ph.D., CSM-L, GISP

What to Do with All Those Numbers?

Using computers to perform complex numerical calculations has become so commonplace that we frequently forget to curb our enthusiasm for "precision" and let the computer just take over. I have had so many GIS students who would report polygon areas to 0.0000001 acres, just because the computer could produce a value. Of course, 0.0000001 acres probably amounts to a teaspoon-full of soil! So, while the computer can calculate those infinitesimally small values, when we display numbers on a map or in a table, we need to be careful and mindful of the precision.

For this month's Tips & Tricks, I'll start with a shapefile containing polygons for the counties of Florida, and in ArcGIS Pro, add a field, SqMi (Square Miles) as a "Double", with the default Number Format as shown in Figure 1. You can also use QGIS or any other GIS software package that can read/write shapefiles.

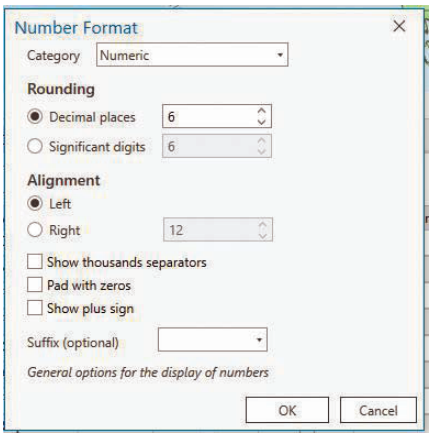

Figure 1. ArcGIS Pro default settings for a "Double" field.

Then I'll calculate the value using the Esri "Calculate Geometry" tool:

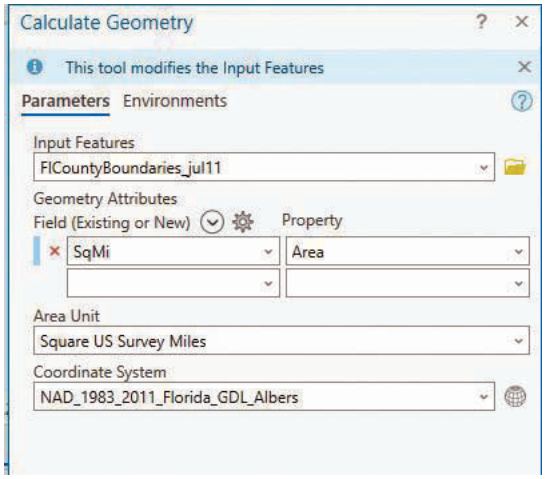

Figure 2. ArcGIS Pro dialog box for calculating the area of the county polygons.

Notice that the values in the table (Figure 3a) are expressed out six significant digits, as specified by the default parameters when creating the field.

While you can change the number of digits displayed in the table by opening the "Fields View" of the table, double-clicking on the Number Format | Numeric cell to expose the ellipses (…) and then adjusting the Rounding | Decimal Places (to two), and Saving your changes, all this does is round the numbers as displayed in the table (Figure 3b) to your specified precision.

When I label the counties using the SqMi field, without respect to the values displayed in the table, I get label values, some of which are showing up to nine significant digits (Figure 4).

To put that into a real-world perspective, 0.000000001 miles would be four square inches! So, this brings up one of the re-occurring themes in this column … Never accept the defaults." In this case, default also clearly demonstrates that it is up to the author of the map to determine the level of precision that is both necessary and appropriate for the data. However, as with everything GIS, there are multiple ways to produce the desired outcome.

I have had so many GIS students who would report polygon areas to 0.0000001 acres, just because the computer could produce a value. Of course, 0.0000001 acres probably amounts to a teaspoon-full of soil!

Photogrammetric Engineering & Remote Sensing
Vol. 90, No. 8, August 2024, pp. 457-461.
0099-1112/22/457-461

doi: 10.14358/PERS.90.8.457

FlCountyBoundaries_jul11

Field: Add Calculate Selection: Select By Attributes Zoom To Switch Clear Delete Copy

	Shape	NAME	FGDLCODE	FIPS	DESCRIPT	FGDLAQDATE	Region	FID	OBJECTID	AUTOID	SqMi
1	Polygon	ALACHUA	C01	001	ALACHUA	4/18/2012	Peninsula	40	34	1	969.50991
2	Polygon	BAKER	C02	003	BAKER	4/18/2012	Peninsula	41	35	2	588.753394
3	Polygon	BAY	C03	005	BAY	4/18/2012	Panhandle	42	36	3	774.584004
4	Polygon	BRADFORD	C04	007	BRADFORD	4/18/2012	Peninsula	35	17	4	300.045559
5	Polygon	BREVARD	C05	009	BREVARD	4/18/2012	Peninsula	36	18	5	1055.463568
6	Polygon	BROWARD	C06	011	BROWARD	4/18/2012	Peninsula	14	19	6	1222.449146
7	Polygon	CALHOUN	C07	013	CALHOUN	4/18/2012	Panhandle	15	20	7	574.34131
8	Polygon	CHARLOTTE	C08	015	CHARLOTTE	4/18/2012	Peninsula	16	21	8	727.348257

Figure 3a. ArcGIS Pro table showing calculated SqMi field displayed to default precision.

FlCountyBoundaries_jul11 Fields: FlCountyBoundaries_jul11

Field: Add Calculate Selection: Select By Attributes Zoom To Switch Clear Delete Copy

	Shape	NAME	FGDLCODE	FIPS	DESCRIPT	FGDLAQDATE	Region	FID	OBJECTID	AUTOID	SqMi
1	Polygon	ALACHUA	C01	001	ALACHUA	4/18/2012	Peninsula	40	34	1	969.51
2	Polygon	BAKER	C02	003	BAKER	4/18/2012	Peninsula	41	35	2	588.75
3	Polygon	BAY	C03	005	BAY	4/18/2012	Panhandle	42	36	3	774.58
4	Polygon	BRADFORD	C04	007	BRADFORD	4/18/2012	Peninsula	35	17	4	300.05
5	Polygon	BREVARD	C05	009	BREVARD	4/18/2012	Peninsula	36	18	5	1055.46
6	Polygon	BROWARD	C06	011	BROWARD	4/18/2012	Peninsula	14	19	6	1222.45
7	Polygon	CALHOUN	C07	013	CALHOUN	4/18/2012	Panhandle	15	20	7	574.34
8	Polygon	CHARLOTTE	C08	015	CHARLOTTE	4/18/2012	Peninsula	16	21	8	727.35

Figure 3b. ArcGIS Pro table showing calculated SqMi field displayed to customized precision.

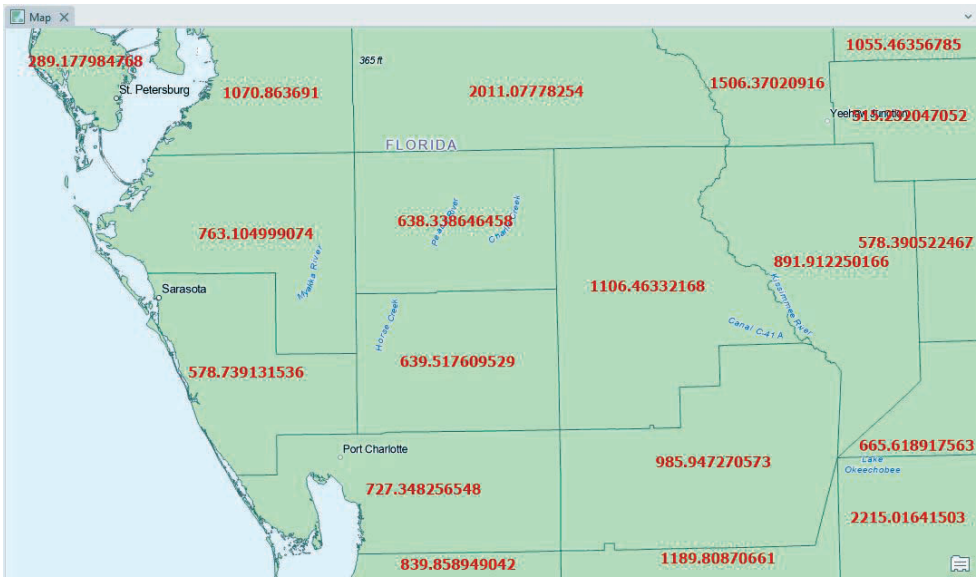

Figure 4. Florida county map labeled by the SqMi field displays default label precision when the table values are customized.

In ArcGIS Pro:

Tip #1 — Quick and Dirty – One "quick and dirty" method to customize the precision displayed in the labels is to create the label as an Integer (i.e., a long) value. This method will round the very precise 32-bit floating value to an integer (i.e., no decimals). So, if you are making a very small-scale map and the numerical values are used as relative indicators, this might be a good solution.

1. If you have not created the SqMi field, just create a new field (SqMiInt; square miles, integer) as an integer field and then calculating the geometry as above, or
2. if you have already created the SqMi field, create the SqMiInt field and calculate SqMiInt = SqMi. In either case, you will get a whole number, i.e., an integer, rounded up (Figure 5), and those integers displayed on the map (Figure 6).

Tip #2 — Methodical and Controlled – While the quick and dirty technique might be sufficient for some small-scale maps, sometimes you might need to take total control of the precision. In a case where you want to report the values to 0.01 square miles (~278,000 square feet, or ~6.4 acres), you need to use the computer precision but in moderation. Once again, in ArcGIS Pro, you need to use the "Round" function, but this time, not in the table, but in the label.

As an example, to display labels with two-digits past the decimal:

1. Label using the SqMi field; it does not matter if you adjusted the table display or not,
2. Right-click on the layer in the Contents pane,
3. Navigate to the Label Properties … to open the Label dialog window,
4. Using the Arcade language and the Round() function, enter a custom expression in the Expression window where two is the number of digits past the decimal that you want to display (Figure 7). In this case, I wanted to display the county area to 0.01 square miles:

The resulting map (Figure 8) shows two significant digits as labels which result from the expression in Figure 7.

FlCountyBoundaries_jul11

Field: Add Calculate Selection: Select By Attributes Zoom To Switch Clear Delete Copy

	FID	Shape	OBJECTID	NAME	FGDLCODE	FIPS	DESCRIPT	AUTOID	FGDLAQDATE	Region	SqMi	SqMiInt
1	40	Polygon	34	ALACHUA	C01	001	ALACHUA	1	4/18/2012	Peninsula	969.50991	970
2	41	Polygon	35	BAKER	C02	003	BAKER	2	4/18/2012	Peninsula	588.753394	589
3	42	Polygon	36	BAY	C03	005	BAY	3	4/18/2012	Panhandle	774.584004	775
4	35	Polygon	17	BRADFORD	C04	007	BRADFORD	4	4/18/2012	Peninsula	300.045559	300
5	36	Polygon	18	BREVARD	C05	009	BREVARD	5	4/18/2012	Peninsula	1055.463568	1055
6	14	Polygon	19	BROWARD	C06	011	BROWARD	6	4/18/2012	Peninsula	1222.449146	1222
7	15	Polygon	20	CALHOUN	C07	013	CALHOUN	7	4/18/2012	Panhandle	574.34131	574
8	16	Polygon	21	CHARLOTTE	C08	015	CHARLOTTE	8	4/18/2012	Peninsula	727.348257	727

Figure 5. Table showing the SqMiInt field as an integer value.

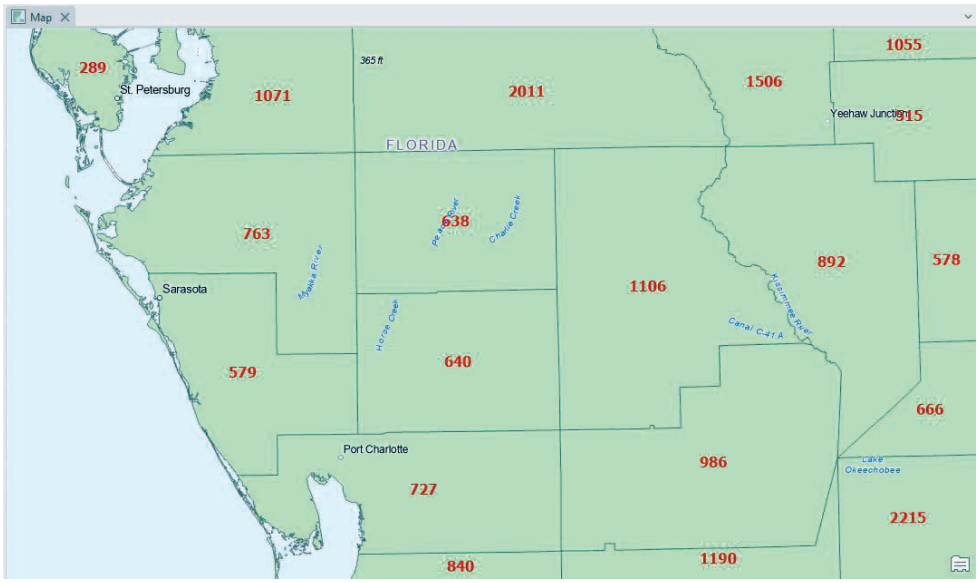

Figure 6. Map of the counties using the SqMiInt field for labels.

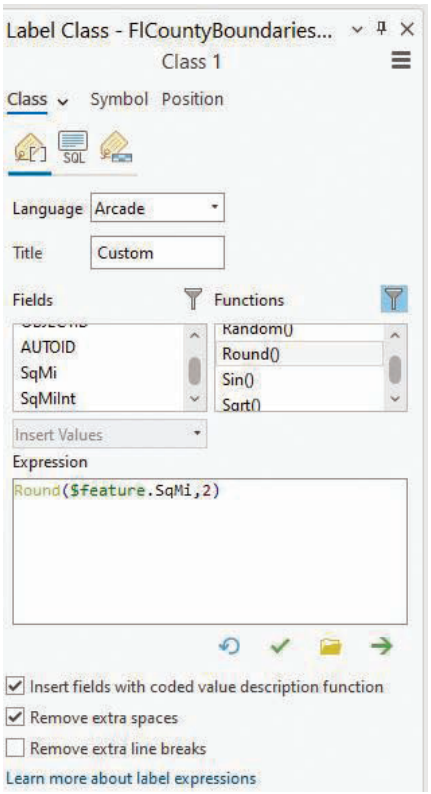

Figure 7. The Label Class dialog box in ArcGIS Pro showing an Arcade expression using the Round() function to specify two decimal places for the displayed labels.

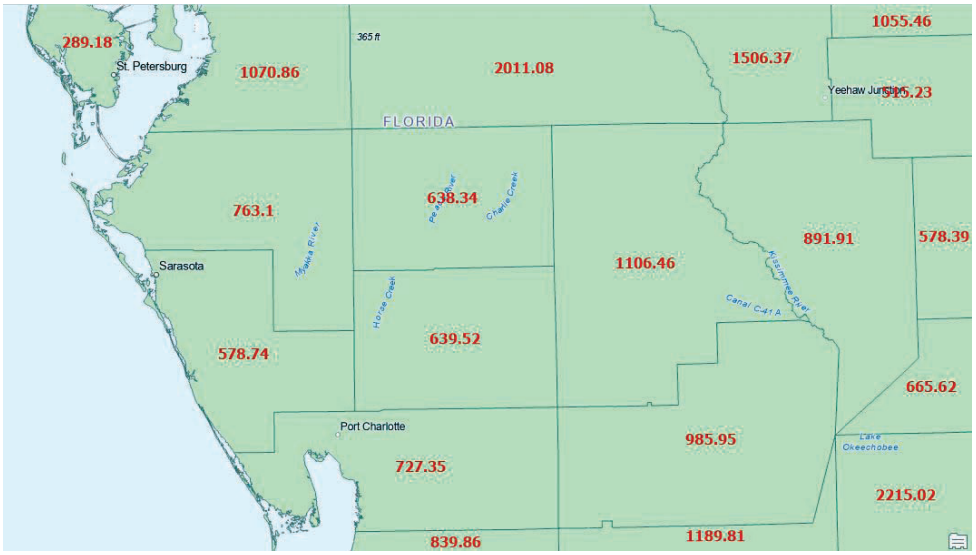

Figure 8. ArcGIS Pro map showing the SqMi field labels as customized using the Arcade expression in Figure 7.

In QGIS (3.32.2-Lima):

Tip #3 — Labels in QGIS - As with ArcGIS Pro, it should not be surprising that by default, QGIS will also display the nine-digit precision in the SqMi field (Figure 9). (Note: Set the field to use for labels by double-clicking on the layer or open the Layer Properties dialog.)

To customize the labels displayed in QGIS for the SqMi field:

1. Once a label field is selected,
2. Use the Labels option on the Layer Properties dialog to change the attributes (font, size, color, precision, etc.) of the labels. Here I changed the color, to red, size to 12 points, and style to bold,
3. Check the 'Formatted numbers" option (on the bottom of the dialog box), and
4. Set the Decimal places to two (Figure 10.)

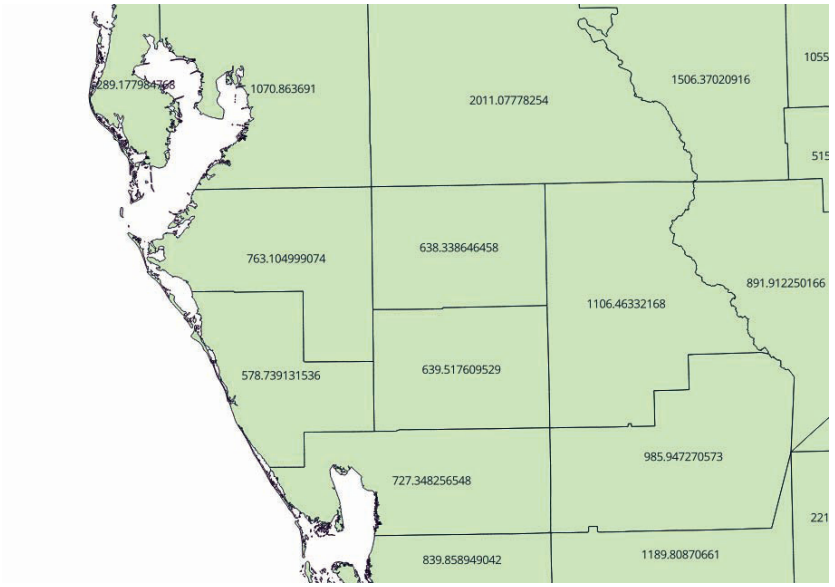

Figure 9. Default labels for the SqMi field displayed in QGIS.

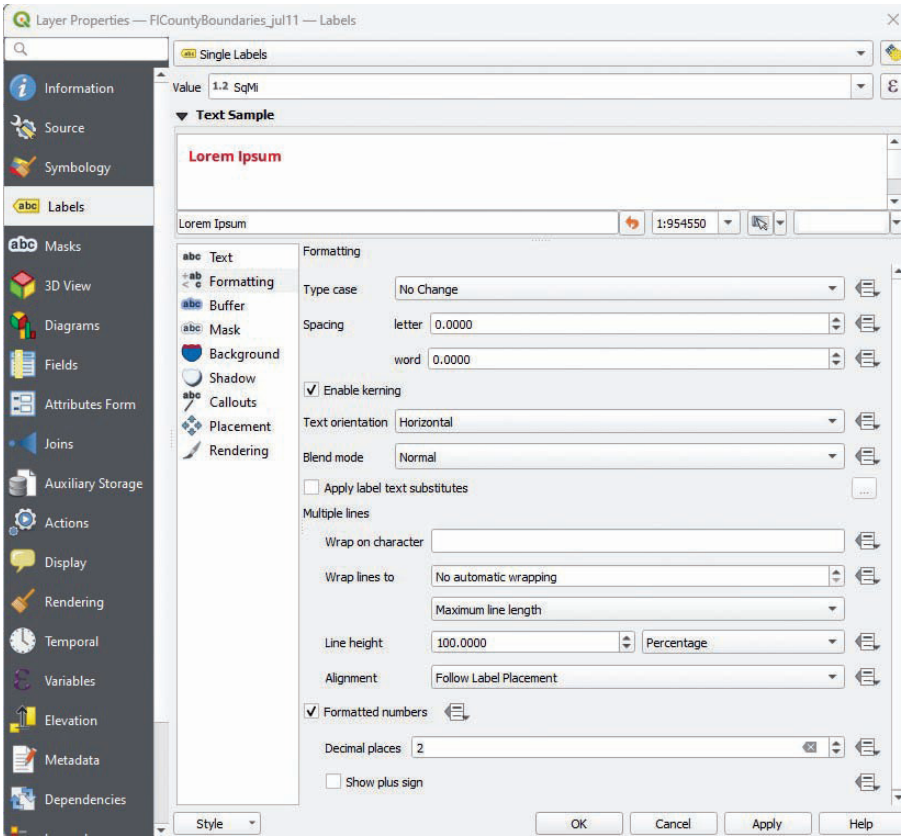

Figure 10. Once a label field is specified in the Display options, use the Label dialog box to customize the displayed values.

The resulting map (Figure 11) displays the customized labels.

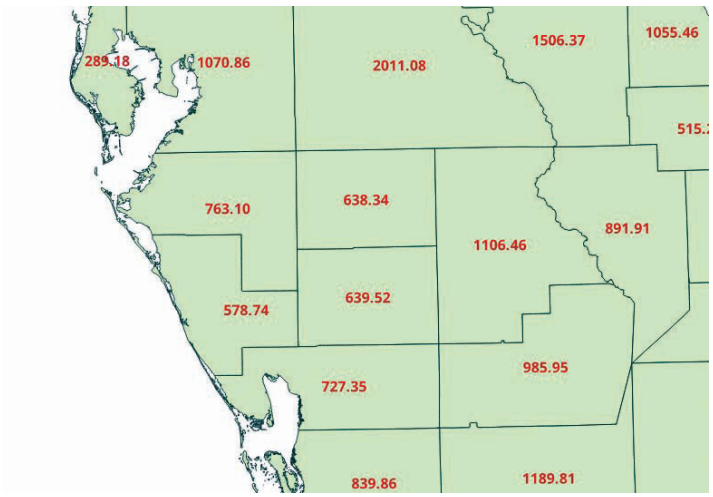

Figure 11. QGIS map showing customized SqMi field value labels.

For general GIS Tips & Tricks send you questions, comments, and tips to: GISTT@ASPRS.org

Al Karlin, Ph.D., CMS-L, GISP is with Dewberry's Geospatial and Technology Services group in Tampa, FL. As a senior geospatial scientist, Al works with all aspects of lidar, remote sensing, photogrammetry, and GIS-related projects.

STAND OUT FROM THE REST

EARN ASPRS CERTIFICATION

ASPRS congratulates these recently Certified and Re-certified individuals:

RECERTIFIED PHOTOGRAMMETRIST

Patrick Moroney, Certification #R1377CP
Effective October 19, 2023, expires October 19, 2028

John Gerhard, Certification #R1236CP
Effective May 7, 2024, expires May 7, 2029

Robert Pakiela, Certification #R1394CP
Effective March 26, 2024, expires March 26, 2029

Raymond Miller, Certification #1645CP
Effective January 23, 2024, expires January 23, 2029

Harold Rempel III, Certification #R1418CP
Effective February 21, 2024, expires February 21, 2029

Darin David, Certification #R1542CP
Effective February 20, 2023, expires February 20, 2028

Angela Livingston, Certification #R1382CP
Effective December 18, 2023, expires December 18, 2028

Brian Tolley, Certification #R1391CP
Effective March 18, 2024, expires March 18, 2029

CERTIFIED PHOTOGRAMMETRIST

Aaron Garibaldi, Certification #CP1677
Effective March 14, 2024, expires March 14, 2029

Nathan Mangsen, Certification #CP1678
Effective April 22, 2024, expires April 22, 2029

Jamen Underwood, Certification #CP1679
Effective April 23, 2024, expires April 23, 2029

CERTIFIED REMOTE SENSING TECHNOLOGIST

Matthew Emmett, Certification #RST244
Effective March 29, 2024, expires March 29, 2027

RECERTIFIED PHOTOGRAMMETRY TECHNOLOGIST

John Ong, Certification #R1578PT
Effective January 1, 2024, expires January 1, 2027

CERTIFIED LIDAR TECHNOLOGIST

Michael Thomas, Certification #LT089
Effective April 15, 2024, expires April 15 2027

Keaton Ford, Certification #LT090
Effective April 21, 2024, expires April 21, 2027

Michael Baranowski, Certification #R062LT
Effective April 1, 2024, expires April 1, 2027

RECERTIFIED MAPPING SCIENTIST REMOTE SENSING

David L. Szymanski, Certification #R163RS
Effective January 27, 2024, expires January 27, 2029

Darin David, Certification #R211RS
Effective February 20, 2023, expires February 20, 2028

RECERTIFIED CERTIFIED MAPPING SCIENTIST GIS/LIS

Edward Kiewel, Certification #R142GS
Effective December 2, 2022, expires December 2, 2027

RECERTIFIED MAPPING SCIENTIST LIDAR

Angela Livingston, Certification #R035L
Effective February 4, 2024, expires February 4, 2029

ASPRS Certification validates your professional practice and experience. It differentiates you from others in the profession. For more information on the ASPRS Certification program: contact **certification@asprs.org,** visit **https://www.asprs.org/general/asprs-certification-program.html.**

asprs THE IMAGING & GEOSPATIAL INFORMATION SOCIETY

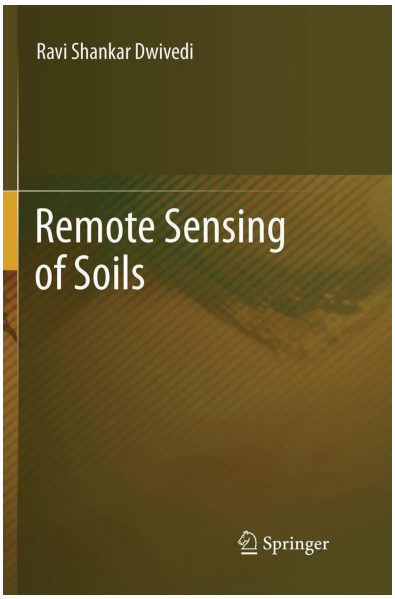

Remote Sensing of Soils

Ravi Shankar Dwivedi
500 pages. 2017. Springer. Hardcover, Paperback and Ebook. ISBN 978-3-662-53738-1.

Reviewed by Pushkar P. Inamdar PhD, Data Scientist, Department of Epidemiology and Biostatistics, University of California San Francisco.

Remote Sensing of Soils by Ravi Shankar Dwivedi is a pivotal work that addresses the critical intersection of modern technology, environmental sustainability, and agricultural innovation. Dwivedi establishes the foundational understanding of remote sensing and its symbiotic relationship with technologies like Geographic Information Systems (GIS), Global Navigation Satellite Systems, and field data collection tools, which form the backbone of contemporary soil management strategies. This enables precise mapping, analysis, and interpretation of soil properties and conditions, essential for addressing global challenges such as food security, resource scarcity, and environmental degradation.

The book excels in two key areas: understanding soil composition and translating remote sensing data into actionable information. The author provides a concise overview of a wide array of airborne and spaceborne datasets, including multispectral, hyperspectral, lidar, and synthetic aperture radar (SAR). These datasets are integral for soil mapping, understanding soil texture and moisture content, and detecting erosion. The author also explores the intriguing science behind soil spectral reflectance patterns, showcasing how these patterns are crucial for deciphering soil properties. This knowledge is then applied to the intricacies of digital soil mapping, where the book highlights the challenges and opportunities in translating raw remote sensing data into actionable soil resource information beneficial for land management practices.

The author's discussion on digital image processing provides a valuable exploration of the techniques for processing spectral measurements from remote sensors. It explores the complexities of creating accurate landscape representations from remote sensing data and examines various image processing methods, including restoration, enhancement, and classification. It covers the Gaussian maximum likelihood classifier, a widely used technique in this field. *Remote Sensing of Soils* also encompasses topics commonly used in image analysis, including techniques like Principal Component Analysis (PCA), image fusion methods, Hierarchical Clustering, the application of Neural Networks in supervised satellite image classification, and object-oriented classifiers, among others. These topics are fundamental in extracting meaningful information from remote sensing data, enabling researchers and practitioners to enhance the accuracy and efficiency of soil mapping, vegetation analysis, and environmental monitoring. The book provides readers with the necessary tools for advanced image-processing tasks.

The later segments of the book examine advanced topics such as soil moisture estimation and soil fertility evaluation, both crucial in modern agriculture and sustainable practices. The author's exploration of remote sensing techniques for assessing these factors showcases the transformative potential of technology in optimizing crop growth and resource utilization.

What sets this book apart is its accessibility and relevance to a diverse audience. Whether one is a seasoned researcher, a technology developer, or a soil science student, Remote Sensing of Soils offers valuable insights and practical knowledge. The author's clear language and comprehensive references make complex concepts understandable and applicable in real-world scenarios.

Future editions of Remote Sensing of Soils might benefit from exploring the potential of machine learning and deep learning in precision agriculture through an introductory chapter. Additionally, showcasing specific applications of geospatial science with machine learning and deep learning techniques in areas like soil moisture estimation, fertility evaluation, and soil classification could further enhance the book's comprehensiveness and relevance for future advancements.

In essence, Remote Sensing of Soils is a valuable roadmap for leveraging advanced technologies like remote sensing, GIS, and geospatial analysis to address critical environmental and agricultural challenges. The book informs readers about the latest advancements and inspires them to explore innovative solutions for sustainable soil management and ecosystem preservation.

Photogrammetric Engineering & Remote Sensing
Vol. 90, No. 8, August 2024, pp. 463.
0099-1112/22/463

doi: 10.14358/PERS.90.8.463

ASPRS APPROVES EDITION 2, VERSION 2 OF THE ASPRS POSITIONAL ACCURACY STANDARDS FOR DIGITAL GEOSPATIAL DATA (2024)

The American Society for Photogrammetry and Remote Sensing (ASPRS) is pleased to announce adoption of the Positional Accuracy Standards for Geospatial Data, Edition 2, Version 2 (2024), which includes important modifications and additions to Edition 2, Version 1 published in August 2023.

Edition 2, Version 2 introduces four new addenda for:

a. Mapping with Lidar.
b. Mapping with Photogrammetry.
c. Mapping with Unmanned Aerial Systems (UAS).
d. Mapping with Oblique Imagery.

Together with the two addenda that were published in Edition 2, Version 1, the Standards offer the mapping community a total of six addenda detailing guidelines and best practices intended to help practitioners perform mapping and create geospatial products that comply with the adopted Standards. As the USGS Lidar Base Specification is well aligned with the ASPRS Positional Accuracy Standards, users of 3DEP data will reap benefits from the modifications introduced in this new version.

Edition 2, Version 2 was adopted after a formal public review period ending April 26, 2024. Public comments were incorporated into the final version adopted by the ASPRS Board of Directors on June 24, 2024.

"The publication of this new edition of the accuracy standards came in response to evolving technologies and industry needs. It will have a positive and lasting impact on geospatial capabilities and all who benefit from these services, here in the United States of America and worldwide. It is a history-making accomplishment that we should all be proud of" said Dr. Qassim Abdullah, Vice President and Chief Scientist of Woolpert, who led the ASPRS Positional Accuracy Standards Working Group. "We are fortunate to have among our members such talented and willing volunteers who worked hard during the last two years to update these important Standards. This latest version represents a collaborative effort by 40 subject matter experts representing public, private, and academic sectors." said Bandana Kar, ASPRS President.

The most significant changes introduced in Edition 2 of the ASPRS Positional Accuracy Standards for Digital Geospatial Data include:

1. Elimination of references to the 95% confidence level as an accuracy measure.
2. Relaxation of the accuracy requirement for ground control and checkpoints.
3. Consideration of survey checkpoint accuracy when computing final product accuracy.

4. Removal of the pass/fail requirement for Vegetated Vertical Accuracy (VVA) for lidar data.
5. Increase the minimum number of checkpoints required for product accuracy assessment from twenty (20) to thirty (30).
6. Limiting the maximum number of checkpoints for accuracy assessment to 120 for large projects.
7. Introduction of a new term, "three-dimensional positional accuracy."
8. Addition of Guidelines and Best Practices Addenda for:
    a. General Guidelines and Best Practices
    b. Field Surveying of Ground Control and Checkpoints
    c. Mapping with Photogrammetry
    d. Mapping with Lidar
    e. Mapping with UAS
    f. Mapping with Oblique Imagery

A more detailed explanation of the Edition 2 changes can be found in the Foreword. To download the complete Standards, visit https://publicdocuments.asprs.org/PositionalAccuracyStd-Ed2-V2 or

The Standards are available in hardcopy format and can be purchased from the ASPRS Bookstore, www.asprs.org.

NEW ASPRS MEMBERS

ASPRS would like to welcome the following new members!

Ophelia Ahmad
Noah Baer
Laura M. Benzan Valette
Dimitrios Bolkas, PhD
William Dunblazier
Sean Hyde, P. Geo
Jerimiah Johnson, Sr.
Prof. Jasmeet Judge
Janeth Ernest Mjema
Sabin Jung Pandey
Kevin Stehman
Jennifer Vasi
Megan Ward-Baranyay
Jie Zhang

FOR MORE INFORMATION ON ASPRS MEMBERSHIP, VISIT
HTTP://WWW.ASPRS.ORG/JOIN-NOW

THE GEOSPATIAL TERMS DEFINED IN THE GLOSSARY OF THE MAPPING SCIENCES HAVE BEEN TRANSLATED INTO ARABIC!

Dr. Mohamed Ahmed Tarabzouni, Consultant to the President of King Abdul-Aziz City for Science and Technology (KACST), Riyadh, Saudi Arabia, translated the terms listed in the Glossary of the Mapping Sciences from English to Arabic.

When asked why he decided to translate the geospatial terminology defined in the Glossary into Arabic, Dr. Tarabzouni responded "This started as a personal project, since my appointment by the UNDP to advocate to other Arab countries to explain the benefits of remote sensing and encourage them to embrace it. Due to the lack of terminology it was extremely difficult to fulfil this. I was selected as the representative of the UNDP, because during the symposium in Tunisia in 1986, I was the only Arab to have a PHD in aerospace engineering and remote sensing.

In 1986 Saudi was building the first Earth observation station in the Middle East with NASA and CNES, the contracts were very difficult to maneuver as they had to be drafted in Arabic, and the lack of terminology made it nearly impossible.

Since I'd been representing the government of Saudi, as the head of the Saudi delegation, in COPUOS since 1984, in New York and Vienna, and the languages of COPUOS are the 6 languages of the United Nations, I found that during the immediate translation there were difficulties for the interpreters, and for many of the technical terms, the English word was used instead of an appropriate translation. "

Dr. Tarabzouni spent three years translating the terminology. Much of which took place during the Covid19 Pandemic. When asked about the value this translation would have to the global geospatial community, he responded, "This is the first translation in the Arab world, available right now to my knowledge as there are currently no specialized dictionaries or glossaries about remote sensing, aerospace engineering and GIS terminology, so the value is intrinsic and will hopefully fill a painful void."

The translation can be downloaded from the Bookstore tab on www.asprs.org.

ASPRS thanks Dr. Tarabzouni for his dedication to the geospatial industry by translating the terminology defined in the Glossary for the Mapping Sciences into Arabic. ASPRS is not responsible for errors or omissions made during the translation process.

Special Issue Introduction
Ushering a New Era of Hyperspectral Remote Sensing to Advance Remote Sensing Science in the Twenty-first Century

Prasad S. Thenkabail, Itiya Aneece, and Pardhasaradhi Teluguntla

Remote sensing science is entering a new era of advanced satellite sensors that, currently and in coming years, provide data in three distinct categories:

1. Hyperspatial data (sub-meter to 5 m spatial resolution) that are often acquired in about 4-10 multispectral broadbands (bandwidths >15 nm) and in 400-12,500 nm portion of the electromagnetic (EM) spectrum.
2. Superspectral data such as from the Landsat Next constellation of three satellites that are acquired typically in 10-60 m, 26 multispectral broadbands (bandwidths >15 nm; but often much broader like 30 to 60 nm) and in 400-12,500 nm portion of the EM spectrum.
3. Hyperspectral data that are acquired in hundreds of narrowbands (bandwidths ≤15 nm) over 400-2500 nm or 400-12,500 nm with spatial resolution of ≤30 m.

All three data types will help advance remote sensing science by providing information in higher spatial, spectral, radiometric, and temporal resolutions. Nevertheless, these large data volumes and complexities bring significant challenges in handling, processing, and analysis. There are, of course, advances in big-data analytics, machine learning, deep learning, artificial intelligence (ML/DL/AI), and cloud computing that help overcome these challenges (Thenkabail *et al.*, 2021a, Thenkabail *et al.*, 2018). However, the greatest challenge offered by these new advanced data is in understanding and developing new science that will help us model, map, and monitor myriad scientific applications. Addressing this challenge requires exploration of the characteristics and limitations of hyperspectral data (Thenkabail *et al.*, 2021a, Thenkabail *et al.*, 2018), superspectral data (Landsat Next, 2024, Wu *et al.*, 2019), and other advanced remote sensing data (Thenkabail *et al.*, 2024) and the opportunities they offer to advance remote sensing science.

In this context, we have assembled a *Photogrammetric Engineering and Remote Sensing* (*PE&RS*) special issue on hyperspectral remote sensing titled "*Ushering a New Era of Hyperspectral Remote Sensing to Advance Remote Sensing Science in the Twenty-first Century*". The goal of the special issue was to solicit scientific papers that advance new science using new- and old- generation hyperspectral data. Great advances are taking place in remote sensing with the advent of new-generation hyperspectral sensors that offer data in hundreds of spectral bands. These include data from already in orbit sensors such as: 1. Germany's Deutsches Zentrum fur Luftund Raumfahrt (DLR's) Earth Sensing Imaging Spectrometer (DESIS) sensor onboard the International Space Station (ISS), 2. Italian Space Agency's (ASI's) PRISMA (Hyperspectral Precursor of the Application Mission), and 3. Germany's DLR's Environmental Mapping and Analysis Program (EnMAP) (Figure 1). Further, Planet Labs PBC will soon launch two hyperspectral sensors called Tanager (Tanager-1 planned for July 2024). NASA is planning the launch of the hyperspectral Surface Biology and Geology (SBG) mission in the coming years. Further, we already have over 83,000+ hyperspectral images of the world acquired from NASA's Earth Observing-1 (EO-1) Hyperion sensor that are freely available to anyone through the U.S. Geological Survey's (USGS) data archives (https://earthexplorer.usgs.gov/). These suites of sensors acquire data in 200 plus hyperspectral narrowbands (HNBs) in 2.55 to 12 nm bandwidth, either in 400-1000 or 400-2,500 nm spectral range with SBG also acquiring data in the thermal range. In addition, Landsat NEXT is planning a constellation of 3 satellites (A, B, C) each acquiring data for 26 bands in the 400-12,000 nm wavelength range (Landsat Next, 2024). HNBs provide data as "spectral signatures," in stark contrast to "a few data points along the spectrum" provided by multispectral broadbands (MBBs), that offer us the opportunity to use hyperspectral data for myriad applications (e.g., Figure 2).

The overarching goal of this special issue was to seek scientific papers that perform research utilizing old and new-generation hyperspectral narrowband (HNB) data and compare their performance with multispectral broadband (MBB) data for a wide array of science applications including methods, techniques, challenges, and advances.

Papers on the following topics were solicited:

1. Methods and techniques of understanding, processing, and computing hyperspectral data with specific emphasis on ML/DL/AI and cloud computing.
2. Issues of hyperspectral data volumes, data redundancy, and overcoming Hughes' phenomenon.
3. Building hyperspectral libraries for purposes of creating reference training, testing, and validation data for land remote sensing applications.
4. Utilizing time-series multispectral and hyperspectral data over many years to build data cubes and apply advanced computational ML/DL/AI methods and approaches on the cloud.
5. Discussions of hyperspectral data analysis techniques like full spectral analysis versus optimal band analysis.
6. Developing hyperspectral vegetation indices (HVIs) for targeted

Photogrammetric Engineering & Remote Sensing
Vol. 90, No. 8, August 2024, pp. 467- 470.
0099-1112/22/467-470

doi: 10.14358/PERS.90.8.467

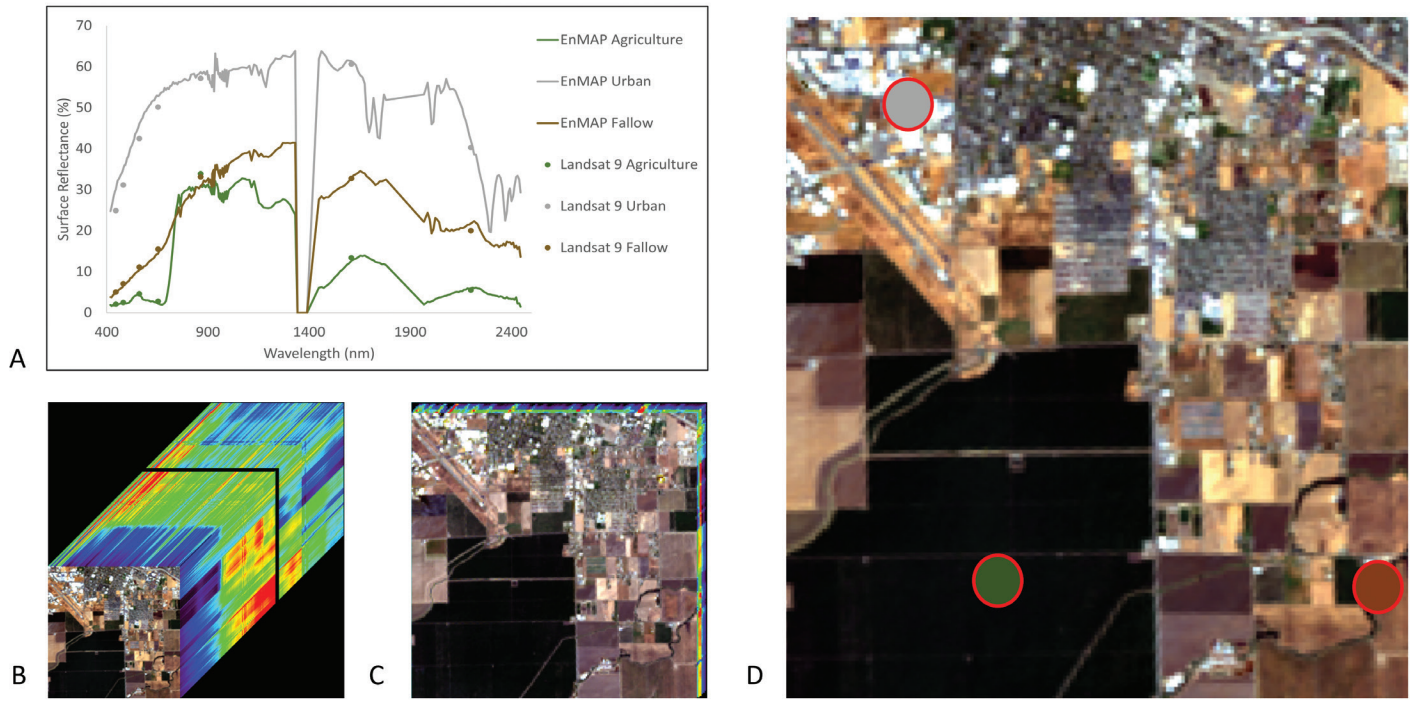

Figure 1. EnMAP Hyperspectral Vs. Landsat 9 Multispectral. A comparison of hyperspectral data from new-generation Germany's DLR's Environmental Mapping and Analysis Program (EnMAP) sensor and multispectral data from USA's NASA's and USGS's Landsat 9. A) Spectral signatures for agriculture, urban, and fallow samples from images acquired in May 2024. B) EnMAP image cube. C) Landsat 9 image cube. D) Sample locations on EnMAP image.Hyperspectral narrowband (HNB) data acquired from new generation Germany's DLR's Environmental Mapping and Analysis Program (EnMAP) sensor that was launched in the year 2022.

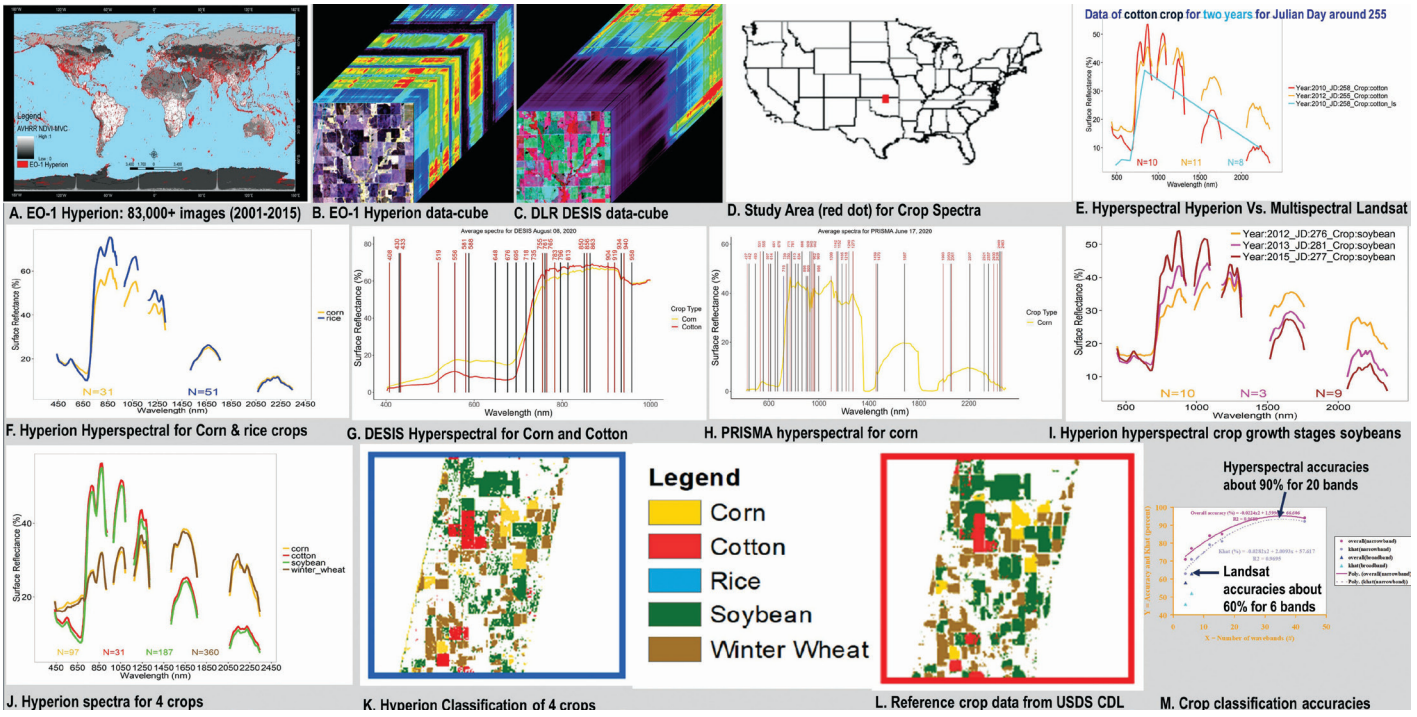

Figure 2. Spectral libraries and crop classifications using old and new generation hyperspectral narrowbands (HNB) data compared with multispectral broadband (MBB) data from Landsat. Old generation hyperspectral data comes from NASA's Earth Observing-1 (EO-1) Hyperion. New generation data comes from German DESIS (DLR Earth Sensing Imaging Spectrometer) and Italian PRISMA (Hyperspectral Precursor of the Application Mission) sensors. The images show Hyperion image distribution over the world (A), Hyperion data-cube (B), DESIS data-cube (C), study area from where crop data are gathered (D), comparison of cotton crop data from hyperspectral Hyperion versus multispectral Landsat (E), spectral libraries of crops from Hyperion (F), DESIS (G), and PRISMA (H), and crop growth stage spectra of soybeans from Hyperion (I). In the last row, crop spectra of 4 crops from Hyperion (J) is shown. The Hyperion image is classified to map these 4 crops (K) and compared with reference data of crops from USDA cropland data layer or CDL (L). The final plot (M) shows classification accuracies that can be achieved in crop classifications using Hyperspectral as opposed to multispectral Landsat [some of the images here are modified and adopted from Aneece and Thenkabail, 2022, Aneece et al., 2022, Aneece and Thenkabail, 2021, and Thenkabail et al., 2021b.

applications to model and map plant biophysical (e.g., yield, biomass, leaf area index), biochemical (e.g., nitrogen, anthocyanins, carotenoids), plant health/stress, and plant structural quantities.

7. Classification of complex vegetation and crop types/species using HNBs and HVIs and comparing them with the performance of multispectral broadband data.

Several papers were submitted for the call, of which those selected will appear in this and subsequent special issues. These papers use advanced hyperspectral data and analysis techniques for various science applications, providing knowledge that will be invaluable in advancing remote sensing science using hyperspectral data and methods (Aneece and Thenkabail, 2022, Aneece *et al.*, 2022, Thenkabail *et al.*, 2021b, Thenkabail *et al.*, 2018).

The paper by Sima Peyghambari *et al.* maps porphyry copper deposits (PCDs) using Italian PRISMA hyperspectral data acquired in 238 hyperspectral narrowbands (HNBs) in 12 nm bandwidth over 400-2500 nm and deep learning neural network (NN) methods. The strength of the paper is the detailed assessments of various NNs for mineral assessments. The methods include: 1. Fully connected neural network (FCNN) model, 2. Convolution neural network (CNN) including 1-dimensional CNN (1D CNN) and 2-dimensional CNN (2D CNN), and 3. Hybrid CNN. The paper compared PRISMA spectra of minerals such as Goethite, Muscovite, Kaolinite, Chlorite, and Calcite and matches with the USGS spectral library of minerals and ground spectra. Peyghambari *et al.* proposed a novel 1D CNN that demonstrated an overall accuracy over 97% in mapping hydrothermal minerals using PRISMA data and helped overcome limitations and uncertainties in other well-known neural network methods.

Hyperspectral Reflectance Assessment for Preliminary Identification of Degraded Soil Zones in Industrial Sites, India by Amitava Dutta *et al.* demonstrates the value of using hyperspectral data in a reconnaissance survey of a large industrial complex for various levels of degraded soil zones. These preliminary studies will help with identifying potential mineral deposits, furthering their studies including ground observations, and exploiting these mineral deposits for extraction and development. The study uses the 212 narrowband data acquired in 400-2500 nm using Germany's EnMAP. One of the greatest strengths of hyperspectral data is their ability to generate (HVIs) (Aneece and Thenkabail, 2022, Thenkabail *et al.*, 2018, Marshall and Thenkabail, 2015, Marshall and Thenkabail, 2014, Mariotto *et al.*, 2013, Thenkabail *et al.*, 2013). Dutta *et al.* use six HVIs to study in soils the water content, salinity, desertification, soil texture, soil composition, and vegetation stress. These 6 HVIs are: 1. Normalized difference water index, 2. Salinity index, 3. Desertification index, 4. Soil clay content index, 5. Iron oxide index, and 6. Vegetation stress index. The paper discusses these indices in detail and highlights their unique abilities to study specific features. The study highlights and discusses spectral matching techniques and various ML algorithms.

Building Shadow Detection Based on Improved Quick Shift Algorithm in GF-2 Images by Yunzhi Chen *et al.* uses sub-meter, 4 broadband hyperspatial data from Chinese Gaofen-2 satellite imagery to map building shadows. The paper explores challenges in utilizing high spatial resolution data. They reduce data redundancy by composing principal component (PC) images where PC1 explains about 80% variance in 4 bands, establishing a brightness component to highlight low brightness values in the shadow region, and developing a normalized difference shadow index to highlight shadows. Also, Chen *et al.* utilize an object-based classification by adopting a quick shift algorithm to break images into homogeneous components and then using a pixel-based random forest (RF) ML algorithm to classify, identify, and map building shadows.

Research Progress of Optical Satellite Remote Sensing Monitoring Asphalt Pavement Aging by Jingwen Wang *et al.* espouses the use of remote sensing data for identifying asphalt pavement aging. The use of hyperspectral libraries of asphalt aging will be an effective and efficient approach to monitoring asphalt aging over large areas. The road reflectivity changes with its age in different portions of the spectrum. For example, the paper shows that the reflectivity of aging asphalt pavement increases significantly from 400 to 680 nm. As asphalt pavement ages, its spectral reflectivity decreases from 860 to 970 nm, while the reflectivity of newly laid asphalt pavement increases. It is important to note that if hyperspectral libraries of asphalt are developed, they can be used as library spectra to match and study changes in spectra over time. This paper highlights the use and need for developing spectral libraries such as USGS mineral spectral library (Kokaly *et al.*, 2017) and the global hyperspectral imaging spectral library of agricultural crops (GHISA) (Mariotto *et al.*, 2020, Thenkabail *et al.*, 2019).

Mapping Winter Wheat Using Ensemble-Based Positive Unlabeled Learning Approach by Hanxiang Wang *et al.* addresses the challenge of separating wheat crop from other similar crops using remote sensing. The authors use nine ML models: Segformer-Batch-Instance-Layer Normalization (BILN) (suggested by authors), DANet, U-Net, Segformer, DeeplabV3+, Weighted Support Vector Machine (WSVM), RF, SVM, and One Class SVM (OCSVM). The BILN demonstrates the positive and unlabeled learning (PUL) method to optimize reference data in image classification to obtain the best results in classifying wheat crop.

Overall, hyperspectral data provide a gigantic leap in remote sensing (Thenkabail *et al.*, 2021b, Thenkabail *et al.*, 2018), bringing tremendous opportunities for advancing remote sensing science by significantly increasing classification accuracies; improving crop biophysical and biochemical modeling; and developing HVIs for specific quantities (e.g., chlorophyll, biomass, crop water, pigments) to be modeled, mapped, and monitored. However, hyperspectral data are not a panacea, unless several challenges such as data volumes, data analysis methods and techniques, Hughes' phenomenon, data redundancy, inter-sensor calibrations (amongst hyperspectral sensors and between hyperspectral and multispectral sensors), and other issues (e.g., developing HVIs for specific quantities) are well understood and addressed. This requires new research using data from new-generation hyperspectral sensors, as exemplified by the papers in this special issue. Numerous other attempts are required by expanding goals and objectives to multiple applications.

Acknowledgements

Any use of trade, firm, or product names is for descriptive purposes only and does not imply endorsement by the U.S. Government.

References

Aneece, I. and P. Thenkabail. 2022. New generation hyperspectral sensor (DESIS and PRISMA) performances in Agriculture. *Photogrammetric Engineering and Remote Sensing*, 88 (11):715-729. https://doi.org/10.14358/PERS.22-00039R2

Aneece, I., D. Foley, P. Thenkabail, A. Oliphant, and T. Pardhasaradhi. 2022. New generation hyperspectral data from DESIS compared and contrasted with hyperspectral resolution Planetscope data for crop type classification. *IEEE Journal of Selected Topics in Applied Earth Observations and Remote Sensing*. Volume: 15 (7846 – 7858). DOI: 10.1109/JSTARS.2022.3204223.

Aneece, I., and P.S. Thenkabail. 2021. Classifying Crop Types Using Two Generations of Hyperspectral Sensors (Hyperion and DESIS) with Machine Learning on the Cloud. *Remote Sensing*. 2021, 13, 4704. https://doi.org/10.3390/rs13224704.

Kokaly, R.F., R.N. Clark, G.A. Swayze, K.E. Livo, T.M. Hoefen, N.C. Pearson, R.A. Wise, W.M. Benzel, H.A. Lowers, R.L. Driscoll, and A.J. Klein. 2017, *USGS Spectral Library Version 7: U.S. Geological Survey Data Series* 1035, 61 p., https://doi.org/10.3133/ds1035.

Landsat Next, 2024. *Fact Sheet*. Fs20243005. USGS Publications Warehouse. DOI: 10.3133/fs20243005. https://www.usgs.gov/publications/landsat-next.

Mariotto, I., P. Thenkabail, and I. Aneece. 2020. *Global Hyperspectral Imaging Spectral-library of Agricultural crops for Central Asia V001* [Data set]. NASA EOSDIS Land Processes Distributed Active Archive Center. Accessed 2024-06-15 from https://doi.org/10.5067/Community/GHISA/GHISACASIA.001

Mariotto, I., P.S. Thenkabail, H. Huete, T. Slonecker, and A. Platonov. 2013. Hyperspectral versus Multispectral Crop- Biophysical Modeling and Type Discrimination for the HyspIRI Mission. *Remote Sensing of Environment*. 139:291-305. IP-049224.

Marshall, M.T. and P.S. Thenkabail. 2015. Advantage of hyperspectral EO-1 Hyperion over multispectral IKONOS, GeoEye-1, WorldView-2, Landsat ETM+, and MODIS vegetation indices in crop biomass estimation. International Society of Photogrammetry and Remote Sensing (ISPRS) *Journal of Photogrammetry and Remote Sensing* (ISPRS P&RS). 108:205–218. http://dx.doi.org/10.1016/j.isprsjprs.2015.08.001.

Marshall, M.T. and P.S. Thenkabail. 2014. Biomass modeling of four leading World crops using hyperspectral narrowbands in support of HyspIRI mission. *Photogrammetric Engineering and Remote Sensing*. 80(4): 757-772.

Thenkabail, P.S. (Editor-in-Chief). 2024. *Remote Sensing Handbook* (Second Edition, Six Volumes). Taylor and Francis Inc.\CRC Press. In Press.

- Volume I: Sensors, Data Normalization, Harmonization, Cloud Computing, and Accuracies
- Volume II: Image Processing, Change Detection, GIS and Spatial Data Analysis
- Volume III: Agriculture, Food Security, Rangelands, Vegetation, Phenology, and Soils
- IV: Forests, Biodiversity, Ecology, LULC and Carbon
- Volume V: Water Resources: Hydrology, Floods, Snow and Ice, Wetlands, and Water
- Volume VI: Droughts, Disasters, Pollution, and Urban Mapping

Thenkabail, P.S., P.G. Teluguntla, J. Xiong, A. Oliphant, R.G. Congalton, M. Ozdogan, M.K. Gumma, J.C. Tilton, C. Giri, C. Milesi, A. Phalke, R. Massey, K. Yadav, T. Sankey, Y. Zhong, I. Aneece, and D. Foley. 2021a, Global cropland-extent product at 30-m resolution (GCEP30) derived from Landsat satellite time-series data for the year 2015 using multiple machine-learning algorithms on Google Earth Engine cloud. *U.S. Geological Survey Professional Paper 1868*, 63 p., https://doi.org/10.3133/pp1868.

Thenkabail, P.S., I. Aneece, P. Teluguntla, and A. Oliphant. 2021b. Hyperspectral Narrowband Data Propel Gigantic Leap in the Earth Remote Sensing. Highlight Article. *Photogrammetric Engineering and Remote Sensing*. http://www.asprs.org/a/publications/pers/2021journals/07-21_July_Flipping_Public.pdf doi: 10.14358/PERS.87.7.461. 87(7): 461-467. IP-127022.

Thenkabail, P.S., G.J. Lyon, and A. Huete, Editors. 2018. *Hyperspectral Remote Sensing of Vegetation* (Second Edition, Four Volume-set). CRC Press-Taylor and Francis group, Boca Raton, London, New York.

- Volume I Title: Fundamentals, Sensor Systems, Spectral Libraries, and Data Mining for Vegetation. . Pp. 296. Hardback ID: 9781138066038; eBook ID: 9781315159331.
- Volume II Title: Hyperspectral Indices and Image Classifications for Agriculture and Vegetation. . Pp. 296. Hardback ID: 9781138066038; eBook ID: 9781315159331.
- Volume III Title: Biophysical and Biochemical Characterization and Plant Species Studies. CRC Press- Taylor and Francis group, Boca Raton, London, New York. Pp. 348. Hardback: 9781138364714.
- Volume IV Title: Advanced Applications in Remote Sensing of Agricultural Crops and Natural Vegetation. Pp. 386. Hardback: 9781138364769; eBook ID: 9780429431166.

Thenkabail, P. and I. Aneece. 2019. Global Hyperspectral Imaging Spectral-library of Agricultural crops for Conterminous United States V001 [Data set]. *NASA EOSDIS Land Processes Distributed Active Archive Center*. Accessed 2024-06-15 from https://doi.org/10.5067/Community/GHISA/GHISACONUS.001.

Thenkabail, P.S., M.K. Gumma, P. Teluguntla, and I.A. Mohammed. 2014. Hyperspectral Remote Sensing of Vegetation and Agricultural Crops. Highlight Article. *Photogrammetric Engineering and Remote Sensing*. 80(4): 697-709. IP-052042.

Wu, Z., G. Snyder, C. Vadnais, R. Arora, M. Babcock, G. Stensaas, P. Doucette, and T. Newman. 2019. User needs for future Landsat missions, *Remote Sensing of Environment*, Volume 231, 2019, 111214, ISSN 0034-4257, https://doi.org/10.1016/j.rse.2019.111214.

Authors

Dr. Prasad S. Thenkabail, pthenkabail@usgs.gov, U. S. Geological Survey (USGS), Flagstaff, Arizona, USA.

Dr. Itiya Aneece, ianeece@usgs.gov, U. S. Geological Survey (USGS), Flagstaff, Arizona, USA.

Dr. Pardhasaradhi Teluguntla, pteluguntla@usgs.gov, Bay Area Environmental Research Institute (BAERI) @ USGS, California, USA.

Research Progress of Optical Satellite Remote Sensing Monitoring Asphalt Pavement Aging

Jingwen Wang, Dayong Yang, Zhiwei Xie, Han Wang, Zhigang Hao, Fanyu Zhou, and Xiaona Wang

Abstract

The aging condition of asphalt pavement is an invaluable basis for traffic infrastructure evaluation. Due to the amount of time and high cost of monitoring and identifying asphalt pavement aging, many current studies focus on satellite remote sensing methods. In this paper, some methods and technologies for monitoring asphalt pavement degradation by optical satellite remote sensing are introduced as a literature review. Many researchers have developed spectrum libraries based on the actual aging of asphalt pavements, and it is possible to construct pavement health indices based on spectrum changes. Some indexes can extract different aging degrees of asphalt pavement from optical satellite images. Of course, current research can only preliminarily reflect the aging phenomenon of asphalt pavement and cannot accurately describe the distress characteristics of asphalt pavement. Future research needs to further strengthen mechanism research, develop higher resolution images, improve image processing technology, and adopt multi-means fusion analysis methods.

Introduction

As an efficient mode of transportation, the highway plays a pivotal role in the development of a national economy. China's highways have developed rapidly in the past 20 years. By the end of 2021, the total length of roads in China had grown to 5.2807 million kilometers. This is an increase of 82 600 kilometers from the end of the previous year. Highway density reached 55.01 km/100 square kilometers, an increase of 0.86 km/100 square kilometers. The length of highway maintenance reached 5.2516 million kilometers, accounting for 99.4% of the total highway mileage (Yin and Mei 2021). Whenever the road surface has problems and cannot be maintained in time, it will cause significant inconvenience to the daily lives of people and the transportation industry. This will put a great deal of pressure on the traffic department to supervise and maintain the road (Cheng *et al.* 2018). Therefore, the rapid investigation and detection of road conditions are of paramount significance for the safe and stable operation of highway traffic (Pan *et al.* 2017). However, different road materials, different road distresses, and different aging degrees of roads will bring considerable management difficulty to road supervision, management, maintenance, and renovation work (Cheng *et al.* 2018; Noronha *et al.* 2002). Therefore, the need for macro and extensive health monitoring and management of roads is becoming increasingly urgent (Cheng *et al.* 2018).

In the early stages of highway development, the survey of road conditions was mainly conducted by road maintenance personnel through manual measurement with instruments (Pan *et al.* 2017). However, the manual detection method is inefficient and destructive to the road surface. With the development of computer and sensor technologies, some advanced sensors and equipment such as onboard laser detectors and image acquisition systems have been used for road condition detection (Chambon and Moliard 2011; Themistocleous *et al.* 2014; Kahn 2021). These devices can obtain real-time road condition information and conduct qualitative diagnosis and quantitative evaluation and analysis to support scientific maintenance decisions (Cline *et al.* 2003; Liq *et al.* 2012; Uddin 2011). Despite these technical means, there are still disadvantages, such as traffic obstruction, high costs, and time-consuming, in addition to the inability to quickly gather road condition information across a whole section of road. Compared with the vehicle-mounted optical monitoring system, it has the disadvantages of limited collection range and limited illumination direction. Satellite earth observation technology, especially high-resolution satellite remote sensing technology, shows great application potential in the application of road condition detection because of its more macroscopic, current, and objective characteristics (Jin 2011; Zhang and Bogus 2014; Mettas *et al.* 2015).

In recent years, a series of studies on road health monitoring using satellite remote sensing images have been carried out successively at home and abroad (Mei *et al.* 2014; Nikolaou 2016). However, in general, current satellite remote sensing technology is relatively rarely applied to road health monitoring. The use of satellite remote sensing means to monitor asphalt pavement aging is still in the preliminary exploration stage (Mettas *et al.* 2016; Schnebele *et al.* 2015). On the one hand, the response mechanism of satellite remote sensing technology to the asphalt pavement aging process is still in the research stage. On the other hand, the use of remote sensing technology and road condition monitoring have not yet formed mature methods and effective quantitative evaluation models (Cheng *et al.* 2018).

In this paper, we summarize the current road condition monitoring methods based on optical satellite remote sensing technology. We analyze the research results and current problems and propose potential directions for future road condition monitoring technology using satellite remote sensing (Pan *et al.* 2017).

Remote Sensing Interpretation Means of Optical Satellite

Optical Satellite Remote Sensing Monitoring Platform

Improving the spectral resolution and spatial resolution of space-borne spectral remote sensing data is the key to promoting satellite remote sensing technology. In the early 1970s, the United States launched terrestrial satellites in only four bands, with an average spectral resolution of 150 nm and a spatial resolution of only 78 m. The *Thematic Mapper* satellite of the 1980s increased to seven bands, with an average spectral resolution of 137 nm in the visible to near-infrared spectrum, and a spatial resolution of 30 m. The French *SPOT* satellite, also launched in the 1980s, has a multispectral resolution of 87 nm and a spatial resolution of 10 m. Since the 1990s, the United States, the European Union, Japan, China, and India have successively launched several hyperspectral satellites. In October 2001, the United States launched the Fast Bird satellite with five bands and a spatial resolution of 0.61 meters. In October 2009, the *WorldView-2* satellite launched by the United States has eight bands and a spatial resolution of 0.5 meters. In December 2011, China launched the *Resource-1 02C* satellite with five bands in space, with a resolution of 2.36 m. In mid-August 2014, the

School of Transportation and Geomatics Engineering, Shenyang Jianzhu University, Shenyang 110168, China.

Corresponding author: Dayong Yang (ydy1120@163.com)

Contributed by Prasad S. Thenkabail, June 19, 2023 (sent for review July 19, 2023; reviewed by Weizhen Hou, Itiya Aneece).

Photogrammetric Engineering & Remote Sensing
Vol. 90, No. 8, August 2024, pp. 471–482.
0099-1112/22/471–482

doi: 10.14358/PERS.23-00045R2

Mapping Winter Wheat Using Ensemble-Based Positive Unlabeled Learning Approach

Hanxiang Wang, Fan Yu, Junwei Xie, Huawei Wan, and Haotian Zheng

Abstract

High-resolution remote sensing images can support machine learning methods to achieve remarkable results in agricultural monitoring. However, traditional supervised learning methods require pre-labeled training data and are unsuitable for non-fully labeled areas. Positive and Unlabeled Learning (PUL), can deal with unlabeled data. A loss function PU-Loss was proposed in this study to directly optimize the PUL evaluation metric and to address the data imbalance problem caused by unlabeled positive samples. Moreover, a hybrid normalization module Batch-Instance-Layer Normalization was proposed to perform multiple normalization methods based on the resolution size and to improve the model performance further. A real-world positive and unlabeled winter wheat data set was used to evaluate the proposed method, which outperformed widely used models such as U-Net, DeepLabv3+, and DA-Net. The results demonstrated the potential of PUL for winter wheat identification in remote sensing images.

Introduction

Winter wheat is one of the important food crops and is closely related to people's healthy lives. Assessing the acreage and distribution of winter wheat timely and accurately can assist in crop management, crop yield estimation, crop disaster warning, and crop planting plan making, which is of great importance to food security and people's livelihood (Liu *et al.* 2019).

Accurate information on the distribution of winter wheat can usually be obtained by assigning professional mappers or experts with relevant expertise to conduct field surveys. Due to the time-consuming and laborious nature of manual surveys, timely mapping of widely distributed winter wheat is still a challenging task (Jean *et al.* 2016).

Remote Sensing (RS) technology, as an important tool for obtaining agricultural and natural resource data in precision agriculture, has been widely used in large-scale crop surveys. RS technology can provide more accurate and timely information on agricultural crops because of its advantages, such as large coverage, less restriction by ground conditions, and short detection period, which has generated great economic and social benefits. High-resolution RS images can reflect the spatial relationship, topology, texture, and fine-grained features in more details, which provides conditions for automated methods to identify winter wheat growing areas(Sun *et al.* 2020).

Many RS classification algorithms, such as the RS index (Qu *et al.* 2021), Support Vector Machine (SVM) (Wei *et al.* 2020), Random Forest (RF) (Mohite *et al.* 2019), and Deep Convolutional Neural Network (DCNN) (Wang *et al.* 2020), can be applied to winter wheat classification. To train and evaluate models, a large number of image-label pairs is required. Unfortunately, generating many segmentation labels for RS images of winter wheat remains challenging. Even with a large amount of RS data support, it is often only possible to use a limited number of labels due to personnel, technology, and funding difficulties.

Supervised learning has been widely used in remote sensing image classification. However, the model performance degrades when the supervised information is not sufficient, since supervised learning assumes that all classes included in the training set are exhaustively labeled. Learning from the data consists of positive and unlabeled examples is called Positive and Unlabeled Learning (PUL). In recent years, PUL-based studies have explored efficient training approaches for Positive and Unlabeled Data Sets (PUD). The goal of both PUL and traditional supervised learning is to train a classifier that distinguishes between positive and negative examples based on the attribute. The difference between supervised learning and PUL is that PUL is a class of algorithms that does not require fully supervised data and all unlabeled samples in the data set are also explicitly considered in the learning process (Bekker and Davis 2020).

By integrating PUL with the winter wheat identification task, this study further explores the advantages of PUL in the classification of RS images with limited label. Inspired by presence and background learning back propagation (PBL-BP) method (Ao *et al.* 2017), this study propose a loss function for end-to-end training of DCNN model without estimating constants from the training set.

We noticed that winter wheat at different growth stages presents different optical appearances, making it challenging to distinguish it from other crops using current methods. Inspired by previous work (Nam and Kim 2019), we introduce a hybrid batch normalization technique called Batch-Instance-Layer Normalization (BILN), which adjusts hybrid ratios at different scales of feature map. This mechanism adapts to variations in winter wheat appearance, allowing for better distinguishing features of winter wheat from other crops.

Appling the DCNN algorithm to the task of winter wheat recognition in the PUL scene, this study proposes an end-to-end winter wheat classification method that considers the learning of both positive and unlabeled samples. The contributions of this paper are as follows:

(1) We convert the evaluation metric of PUL into a general PUL loss function, which allows the model to optimize the evaluation metric of PUL directly. We weighted it with cross-entropy loss and mean-absolute-error loss, and the mixed loss function is called PU-Loss. The DCNN model trained with PU-Loss can achieve higher classification performance.

(2) To adapt to the characteristics of winter wheat appearance changes under different scenes and growth periods, we propose a hybrid normalization method and deploy it on DCNN models with different size resolutions. The branches are called BILN. Experiments show that the proposed method adapts to the winter wheat appearance changes in different growth periods and has the highest test performance.

Hanxiang Wang, Fan Yu, Junwei Xie, and Haotian Zheng are with the Geomatics and Urban Spatial Informatics, Beijing University of Civil Engineering and Architecture.

Huawei Wan is with the Satellite Application Center for Ecology and Environment, Ministry of Ecology and Environment.

Corresponding author: Fan Yu (yufan@bucea.edu.cn)

Contributed by Tolga Bakirman, May 23, 2023 (sent for review September 11, 2023; reviewed by Cary Cox, Itiya Aneece).

Photogrammetric Engineering & Remote Sensing
Vol. 90, No. 8, August 2024, pp. 483–491.
0099-1112/22/483–491

doi: 10.14358/PERS.23-00038R2

WHO'S WHO IN ASPRS

Founded in 1934, the American Society for Photogrammetry and Remote Sensing (ASPRS) is a scientific association serving thousands of professional members around the world. Our mission is to advance knowledge and improve understanding of mapping sciences to promote the responsible applications of photogrammetry, remote sensing, geographic information systems (GIS) and supporting technologies.

BOARD OF DIRECTORS

BOARD OFFICERS

President
Bandana Kar
U. S. Department of Energy (DOE)

President-Elect
Amr Abd-Elrahman
University of Florida

Vice President
Alvan Karlin, PhD, CMS-L, GISP
Dewberry

Past President
Lorraine B. Amenda, PLS, CP
Towill, Inc

Treasurer
John McCombs
NOAA

Secretary
Harold Rempel
ESP Associates, Inc.

COUNCIL OFFICERS

ASPRS has six councils. To learn more, visit https://www.asprs.org/Councils.html.

Sustaining Members Council
Chair: Paul Badr
Deputy Chair: Melissa Martin

Technical Division Directors Council
Chair: Hope Morgan
Deputy Chair: Tao Liu

Early-Career Professionals Council
Chair: Greg Stamnes

Region Officers Council
Chair: Demetrio Zourarakis
Deputy Chair: Cody Condron

Committee Chairs Council
Chair: David Day

Student Advisory Council
Chair: Oscar Duran
Deputy Chair: Ali Alruzuq

TECHNICAL DIVISION OFFICERS

ASPRS has seven professional divisions. To learn more, visit https://www.asprs.org/Divisions.html.

Geographic Information Systems Division
Director: Jin Lee
Assistant Director: Michael Baranowski

Lidar Division
Director: Matt Bethel
Assistant Director: Nora May

Photogrammetric Applications Division
Director: Hank Theiss
Assistant Director: Jae Sung Kim

Primary Data Acquisition Division
Director: Srini Dharmapuri
Assistant Director: Ravi Soneja

Professional Practice Division
Director: Hope Morgan
Assistant Director: Christian Stallings

Remote Sensing Applications Division
Director: Tao Liu
Assistant Director: Indu Jeyachandran

Unmanned Autonomous Systems (UAS)
Director: Bahram Salehi
Assistant Director: Rebecca Capps

REGION PRESIDENTS

ASPRS has 13 regions to serve the United States. To learn more, visit https://www.asprs.org/regions.html.

Alaska Region
Dave Parret

Cascadia Region
Jimmy Schulz

Eastern Great Lakes Region
Craig Fry

Florida Region
Matt LaLuzerne

Gulf South
Cody Condron

Heartland Region
Whit Lynn

Mid-South Region
David Hughes

North Atlantic Region
Kurt Lutz

Northeast Region
Trevis Gigliotti

Pacific Southwest Region
Omar Mora

Potomac Region
Jason Brown

Rocky Mountain Region
Trent Casi

Western Great Lakes Region
Adam Smith

Building Shadow Detection Based on Improved Quick Shift Algorithm in GF-2 Images

Yunzhi Chen, Chao Wang, Wei Wang, Xiang Zhang, and Nengcheng Chen

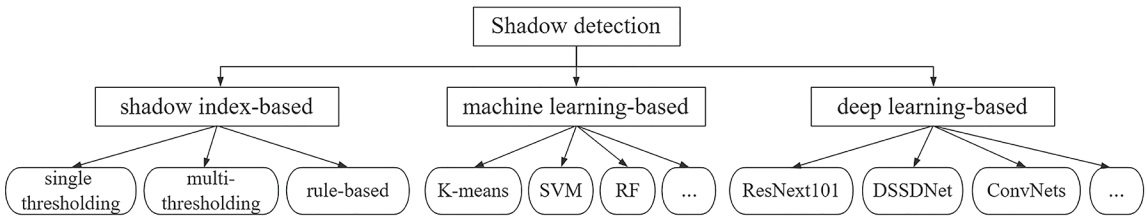

Figure 1. Shadow detection method. The shadow detection method can be divided into three categories: shadow index–based, machine learning–based, and deep learning–based methods. ConvNet = convolutional deep neural network; DSSDNet = deep supervised convolutional neural network; RF = random forest; SVM = support vector machine.

Abstract

Shadows in remote sensing images contain crucial information about various features on the ground. In this study, a method for detecting building shadows in GF-2 images based on improved quick shift was proposed. First, six feature variables were constructed: first principal component (PC1), brightness component (I), normalized difference shadow index (NDSI), morphological shadow index (MSI), normalized difference water index (NDWI), and normalized difference vegetation index (NDVI). Then, the image was segmented to obtain homogeneous objects, which were then classified using a random forest model. Two improvements were added to the quick shift algorithm: using PC1, I, and MSI as input data instead of RGB images; and adding Canny edge constraints. Validation in six research areas yields Kappa coefficients of 0.928, 0.896, 0.89, 0.913, 0.879, and 0.909, confirming method feasibility. In addition, comparative experiments demonstrate its effectiveness and robustness across different land cover types while mitigating the segmentation scale effect.

Introduction

Shadows are a common element in remote sensing images and are caused by buildings, mountains, trees, and other ground objects blocking sun rays, resulting in the backlight of these ground objects forming a dark region in remote sensing images. Shadows can be classified into three categories according to the object causing the shadow: cloud, topographic, and urban shadows. The primary shadow types in remote sensing images vary across different resolutions: topography shadows and cloud shadows are the main shadows in low-resolution images, but urban shadows are the main shadow in high-resolution remote sensing images (Mostafa 2017).

Due to the popularity of high-resolution remote sensing images, many scholars use them to extract information and conduct various studies. However, the existence of shadows causes radiation distortion, confusing the original spectral feature of the images. Thus, the quality of information extracted from the images is reduced (Alavipanah *et al.* 2022), affecting studies on target detection, terrain classification, automatic driving, target tracking, and other applications. However, many scholars obtain ground object information from the shadow area. For instance, the shadows cast by buildings can provide valuable insights into their height and structure. These data can be used to calculate the urban floor area ratio, making it highly significant for city planning and development. Therefore, the detection and removal of shadows has attracted increasing attention from scholars.

Whether the goal is to use shadows to extract information or remove the influence they cause, shadow detection is the first issue to be addressed. At present, many scholars have conducted studies on shadow detection, proposing various shadow detection methods. These remote sensing image-based shadow detection methods are categorized, with results shown in Figure 1. They can be divided into three categories: shadow index–based methods, machine learning–based methods, and deep learning–based methods.

Manual specification of shadow features is necessary in both the shadow index–based method and the traditional machine learning–based method. These features can be directly derived from the band features in the original remote sensing image or obtained through other means. For example, Wang *et al.* (2019) converted RGB color space to HSV color space to obtain better shadow features; Hui and Tianwen (2013) used principal component analysis to obtain the first principal component (PC1) as the shadow feature; Liu *et al.* (2020) extracted the texture feature of the image as one of the shadow features; Fu *et*

Yunzhi Chen is with the State Key Laboratory of Information Engineering in Surveying, Mapping and Remote Sensing, Hubei Luojia Laboratory, Wuhan University.

Chao Wang is with the State Key Laboratory of Information Engineering in Surveying, Mapping and Remote Sensing, Hubei Luojia Laboratory, Wuhan University (c.wang@whu.edu.cn).

Wei Wang is with the State Key Laboratory of Information Engineering in Surveying, Mapping and Remote Sensing, Hubei Luojia Laboratory, Wuhan University.

Xiang Zhang is with the National Engineering Research Center of Geographic Information System, China University of Geosciences.

Nengcheng Chen is with the National Engineering Research Center of Geographic Information System, China University of Geosciences.

Corresponding author: Chao Wang (c.wang@whu.edu.cn)

Contributed by Prasad S. Thenkabail, October 28, 2023 (sent for review January 4, 2024; reviewed by Weiwei Sun, Pardhasaradhi Teluguntla).

Photogrammetric Engineering & Remote Sensing
Vol. 90, No. 8, August 2024, pp. 493–502.
0099-1112/22/493–502

doi: 10.14358/PERS.23-00079R2

Hyperspectral Reflectance Assessment for Preliminary Identification of Degraded Soil Zones in Industrial Sites, India

Amitava Dutta, Rashi Tyagi, Shilpi Sharma, and Manoj Datta

Abstract

The study explores the potential of next-generation satellite hyperspectral imaging systems for screening and predicting surface-soil contamination and degradation by exploiting various spectral indices and signature-matching techniques at a heavily industrialized area in India. The soil moisture content, desertification and salinity status, clay or fine material content, heavy metal content, vegetation health status, and stress levels were assessed from continuum-removed spectral reflectance values. Results indicated the presence of water in two tailings ponds, high salinity, and desertification values in most of the tailings ponds and dump sites, clay boundary liner along four ponds, high heavy metal indices along three ponds and all dump sites, highly stressed vegetation near all tailings ponds and coal dump sites, and pollutants in nearby water channels. The results suggest a strategy for the initial identification of priority areas for ground-based investigations and an alternative rapid methodology to monitor large industrial hubs in India.

Introduction

Mapping of industrial byproducts or residues through their mineral composition at various sites, specifically in developing countries, is a topic of increasing interest because the residues are often high-risk factors for land, water, and air pollution. Fine industrial residue dust with inorganic pollutants and heavy metal traces could adversely affect human health and cause cancer if not mitigated strategically. The nature of the industry and the level of the industry's economic activities are indicated by monitoring physiochemical components of industrial byproducts, which in turn assists in developing a system with an efficient and transparent environmental effect assessment and fair taxation. The industrial byproducts or residues can be reused and recycled under the framework of a cyclic economy, which could include reducing the consumption of virgin raw materials in the construction industry, landfilling and road development, and agricultural activities. Using this context, the exact nature and physiochemical characteristics of industrial byproducts or residues are critical when determining efficient reuse and recycling practice within the United Nations 17 Sustainable Development Goals.

The characteristics of industrial byproducts or residues in tailings ponds or dump sites are mostly determined through extensive ground sampling and subsequent wet chemistry or laboratory analysis. Dump site characterization also involves interpolating quality parameters at nonsampled points within the site. These processes are expensive, time consuming, tedious, and sometimes subjective. Monitoring diversified large industrial hubs through traditional techniques is unsustainable for a fast-developing economy such as India. Remote sensing technologies—specifically satellite hyperspectral imaging—could provide rapid, precise, and economical monitoring of various industrial hubs and their effect on the surrounding environment while also identifying policy gaps at the regional level (Choe *et al.* 2008; Pascucci *et al.* 2012; Marion and Carrère 2018; Stankevich *et al.* 2018; Wan *et al.*; Zahra *et al.* 2024).

In recent decades, by diagnosing spectral signature characteristics of numerous materials, hyperspectral imaging has proven to be a powerful and precise tool for environmental monitoring (Pabon *et al.* 2019; Aneece and Thenkabail 2022; Shaik *et al.* 2023; Dutta *et al.* 2024). Hyperspectral imaging has allowed researchers to exploit distinct spectral absorption features—including their relative strength and shape—for precise identification and mapping of the spatial distribution of several pollutants (Swayze *et al.* 2000; Mars and Crowley 2003; USGS 2005; Pascucci *et al.* 2012; Zahra *et al.* 2024).

Researchers have adopted diversified approaches (e.g., spectral indices) typically developed using normalized band ratioing at absorption features (Asadzadeh and Filho 2016; Dutta *et al.* 2023), spectral signature library-matching techniques (Clark *et al.* 2003; Pascucci *et al.* 2012; Marion and Carrère 2018; Pabon *et al.* 2019), physically based approaches (e.g., modified Gaussian model; Sunshine and Pieters 1993; Sunshine *et al.* 1990; Brossard *et al.* 2016), and, more recently, machine- and deep-learning techniques for characterization of industrial and mining tailings using hyperspectral imageries (Wang *et al.* 2021; Sun *et al.* 2023; Wang *et al.* 2023).

Choe *et al.* (2008) exploited the spectral signature variations due to the presence of heavy metals in soils to map the spatial distribution in a mining tailings area in Spain. The absorption features of several heavy metals (Al, Cr, and Fe) were combined with ground samples to develop spectral indices–based predictive models for heavy metal contamination. Pascucci *et al.* (2012) found that aerial hyperspectral images can efficiently detect red mud dust residue of aluminum-extraction plants using unsupervised and spectral shape–based analysis techniques. They suggested adopting a similar approach for rapidly detecting industrial waste to support the development of preventive policies.

Marion and Carrère (2018) deployed an automatized Gaussian model on aerial hyperspectral images to map spectral characteristics at two different industrial plants in France. They found that hyperspectral imagery-based signatures can efficiently distinguish several industrial pollutants; the results were consistent with in situ measurements. Stankevich *et al.* (2018) successfully mapped radioactive pollution

Amitava Dutta and Shilpi Sharma are with the School of Interdisciplinary Research (SIRe), Indian Institute of Technology Delhi, New Delhi, India (srz218571@iitd.ac.in).

Rashi Tyagi and Shilpi Sharma are with the Department of Biochemical Engineering and Biotechnology, Indian Institute of Technology Delhi, New Delhi, India.

Manoj Datta is with the Department of Civil Engineering, Indian Institute of Technology Delhi, New Delhi, India.

Corresponding author: Amitava Dutta (srz218571@iitd.ac.in)

Contributed by Prasad S. Thenkabail, January 7, 2024 (sent for review February 20, 2024; reviewed by Itiya Aneece, Adam Oliphant, Pardhasaradhi Teluguntla, Nilton Imai).

Photogrammetric Engineering & Remote Sensing
Vol. 90, No. 8, August 2024, pp. 503–509.
0099-1112/22/503–509

doi: 10.14358/PERS.24-00005R2

Marion, R. and V. Carrère. 2018. Mineral mapping using the automatized gaussian model (AGM)—Application to two industrial French sites at Gardanne and Thann. *Remote Sensing* 10:146.

Mars, J. C. and J. K. Crowley. 2003. Mapping mine wastes and analyzing areas affected by selenium-rich water runoff in southeast Idaho using AVIRIS imagery and digital elevation data. *Remote Sensing of Environment* 84:422–436.

NV5 Geospatial Solutions. 2024. *ENVI* version 5.6. Agricultural Stress Tool. https://www.nv5geospatialsoftware.com/docs/AgriculturalStressTool.html

OpenStreetMap contributors. OpenStreetMap database. OpenStreetMap Foundation: Cambridge, UK; 2023. © OpenStreetMap contributors. Available under the Open Database Licence from: openstreetmap.org.

Pabon, R.E.C., C.R.S. Filho and W. J. Oliveira. 2019. Reflectance and imaging spectroscopy applied to detection of petroleum hydrocarbon pollution in bare soils. *Science of Total Environment* 649:1224–1236.

Pascucci, S., C. Belviso, R. M. Cavalli, A. Palombo, S. Pignatti and F. Santini. 2012. Using imaging spectroscopy to map red mud dust waste: The Podgorica aluminum complex case study. *Remote Sensing of Environment* 123:139–154.

Segal, D. 1982. Theoretical basis for differentiation of ferric-iron bearing minerals, using Landsat MSS data, *Proceedings of Symposium for Remote Sensing of Environment, Second Thematic Conference on Remote Sensing for Exploratory Geology*, Fort Worth, Texas, pp. 949–951.

Shaik, R. U., S. Periasamy and W. Zeng. 2023. Potential Assessment of PRISMA Hyperspectral Imagery for Remote Sensing Applications. *Remote Sensing* 15:1378.

Stankevich, S. A., M. M. Kharytonov, A. A. Kozlova, V. Y. Korovin, M. O. Svidenyuk and A. M. Valyaev. 2018. Soil contamination mapping with hyperspectral imagery: Pre-Dnieper chemical plant (Ukraine) case study. In *Hyperspectral Imaging in Agriculture, Food and Environment*. Edited by Alejandro Isabel Luna Maldonado, Humberto Rodríguez Fuentes and Juan Antonio Vidales ContrerasIntechOpen, pp. 121-136. https://doi.org/10.5772/intechopen.70213.

Sun, Y., S. Chen, X. Dai, D. Li, H. Jiang and K. Jia. 2023. Coupled retrieval of heavy metal nickel concentration in agricultural soil from spaceborne hyperspectral imagery. *Journal of Hazardous Materials* 446:130722.

Sunshine, J. M. and C. M. Pieters. 1993. Estimating modal abundances from the spectra of natural and laboratory pyroxene mixtures using the modified gaussian model. *Journal of Geophysical Research: Planets* 98:9075–9087.

Sunshine, J. M., C. M. Pieters and S. F. Pratt. 1990. Deconvolution of mineral absorption bands: An improved approach. *Journal of Geophysical Research: Planets*, 95:6955–6966.

Swayze, G. A., K. S. Smith, R. N. Clark, S. J. Sutley, R. M. Pearson, J. S. Vance, P. L. Hageman, P. H. Briggs, A. L. Meier, M. J. Singleton and S. Roth. 2000. Using imaging spectroscopy to map acidic mine waste. *Environmental Science and Technology* 34:47–54.

U.S. Geological Survey (USGS). 2005. Remote sensing for environmental site screening and watershed evaluation in Utah mine lands east Tintic mountains, Oquirrh mountains, and Tushar mountains. *U.S. Geological Survey scientific investigations report 2004-5241*: 3-31, USGS, Denver, Colorado, USA.

Wang, L. and J. Qu. 2007. NMDI: A normalized multi-band drought index for monitoring soil and vegetation moisture with satellite remote sensing. *Geophysical Research Letters* 34:L20405.

Wang, M., C. Wang, J. Ruan, W. Liu, Z. Huang, M. Chen and B. Ni. 2023. Pollution level mapping of heavy metal in soil for ground-airborne hyperspectral data with support vector machine and deep neural network: A case study of Southwestern Xiong'an, China. *Environmental Pollution* 321:121132.

Wang, Y., H. Ma, J. Wang, L. Liu, M. Pietikäinen, Z. Zhang and X. Chen. 2021. Hyperspectral monitor of soil chromium contaminant based on deep learning network model in the Eastern Junggar coalfield. *Spectrochimica Acta Part A: Molecular and Biomolecular Spectroscopy* 257:119739.

Wan, Y., X. Hu, Y. Zhong, A. Ma, L. Wei, and L. Zhang. 2019. Tailings reservoir disaster and environmental monitoring using the UAV-ground hyperspectral joint observation and processing: A case of study in Xinjiang, the Belt and Road, *IGARSS 2019: 2019 IEEE International Geoscience and Remote Sensing Symposium*, 28 July–2 August 2019, Yokohama, Japan, pp. 9713–9716.

Zahra, A., R. Qureshi, M. Sajjad, F. Sadak, M. Nawaz, H. A. Khan and M. Uzair. 2024. Current advances in imaging spectroscopy and its state-of-the-art applications. *Expert Systems with Applications* 238:122172.

In-Press Articles

Development of an Automatic Feature Point Classification Method for Three-Dimensional Mapping Around Slewing and Derricking Cranes. *Hisakazu Shigemori, Junichi Susaki, Mizuki Yoneda, and Marek Ososinski.*

Semantic Segmentation of Point Cloud Scene via Multi-Scale Feature Aggregation and Adaptive Fusion. *Baoyun Guo, Xiaokai Sun, Cailin Li, Na Sun, Yue Wang, and Yukai Yao.*

A Robust Star Identification Algorithm for Resident Space Object Surveillance. *Liang Wu, Pengyu Hao, Kaixuan Zhang, Qian Zhang, Ru Han, and Dekun Cao.*

Wavelets for Self-Calibration of Aerial Metric Camera Systems. *Jun-Fu Ye, Jaan-Rong Tsay, and Dieter Fritsch.*

Attention Heat Map-Based Black-Box Local Adversarial Attack for Synthetic Aperture Radar Target Recognition. *Xuanshen Wan, Wei Liu, Chaoyang Niu, and Wanjie Lu.*

Exploring the Potential of the Hyperspectral Remote Sensing Data China Orbita Zhuhai-1 in Land Cover Classification. *Caixia Li, Xiaoyan Xiong, Lin Wang, Yunfan Li, Jiaqi Wang, and Xiaoli Zhang.*

Teacher-Student Prototype Enhancement Network for a Few-Shot Remote Sensing Scene Classification. *Ye Zhu, Shanying Yang, and Yang Yu.*

SUSTAININGMEMBERS

Aerial Services, Inc.
Cedar Falls, Iowa
www.AerialServicesInc.com
Member Since: 5/2001

Applanix
Richmond Hill, Ontario, Canada
http://www.applanix.com
Member Since: 7/1997

Ayres Associates
Madison, Wisconsin
www.AyresAssociates.com
Member Since: 1/1953

Dewberry
Fairfax, Virginia
www.dewberry.com
Member Since: 1/1985

Digital Mapping, Inc.(DMI)
Huntington Beach, California
www.admap.com
Member Since: 4/2002

Environmental Research Incorporated
Linden, Virginia
www.eri.us.com
Member Since: 8/2008

Esri
Redlands, California
www.esri.com
Member Since: 1/1987

GeoCue Group
Madison, Alabama
http://www.geocue.com
Member Since: 10/2003

GeoDyn GmbH
Munich, Germany
www.geodyn.com/index
Member Since: 3/2024

Geographic Imperatives LLC
Centennial, Colorado
Member Since: 12/2020

GPI Geospatial Inc.
Orlando, Florida
www.aca-net.com
Member Since: 1/1994

Halff Associates, Inc.
Richardson, Texas
www.halff.com
Member Since: 8/2021

Keystone Aerial Surveys, Inc.
Philadelphia, Pennsylvania
www.kasurveys.com
Member Since: 1/1985

Kucera International
Willoughby, Ohio
www.kucerainternational.com
Member Since: 1/1992

L3Harris Technologies
Broomfield, Colorado
www.l3harris.com
Member Since: 6/2008

Merrick & Company
Greenwood Village, Colorado
www.merrick.com
Member Since: 4/1995

Miller Creek Associates
SeaTac Washington
www.mcamaps.com
Member Since: 12/2014

Nearmap
South Jordan, Utah
www.nearmap.com
Member Since: 6/2023

NV5 Geospatial
Sheboygan Falls, Wisconsin
www.quantumspatial.com
Member Since: 1/1974

Pickett and Associates, Inc.
Bartow, Florida
www.pickettusa.com
Member Since: 4/2007

PixElement
Belmont, Michigan
https://pixelement.com
Member Since: 2/2017

Riegl USA, Inc.
Orlando, Florida
www.rieglusa.com
Member Since: 11/2004

RRC International, LLC
Round Rock, Texas
https://rrccompanies.com/
Member Since: 9/2023

Sanborn Map Company
Colorado Springs, Colorado
www.sanborn.com
Member Since: 10/1984

Surdex Corporation
(a Bowman company)
Chesterfield, Missouri
www.surdex.com
Member Since: 12/2011

Surveying And Mapping, LLC (SAM)
Austin, Texas
www.sam.biz
Member Since: 12/2005

T3 Global Strategies, Inc.
Bridgeville, Pennsylvania
https://t3gs.com/
Member Since: 6/2020

Towill, Inc.
San Francisco, California
www.towill.com
Member Since: 1/1952

Woolpert LLP
Dayton, Ohio
www.woolpert.com
Member Since: 1/1985

SUSTAININGMEMBER**BENEFITS**

Membership

- ✓ Provides a means for dissemination of new information
- ✓ Encourages an exchange of ideas and communication
- ✓ Offers prime exposure for companies

Benefits of an ASPRS Membership

- Complimentary and discounted Employee Membership*
- E-mail blast to full ASPRS membership*
- Professional Certification Application fee discount for any employee
- Member price for ASPRS publications
- Discount on group registration to ASPRS virtual conferences
- Sustaining Member company listing in ASPRS directory/website
- Hot link to company website from Sustaining Member company listing page on ASPRS website
- Press Release Priority Listing in *PE&RS* Industry News
- Priority publishing of Highlight Articles in *PE&RS* plus, 20% discount off cover fee
- Discount on *PE&RS* advertising
- Exhibit discounts at ASPRS sponsored conferences (exception ASPRS/ILMF)
- Free training webinar registrations per year*
- Discount on additional training webinar registrations for employees
- Discount for each new SMC member brought on board (Discount for first year only)

One-Dimensional-Mixed Convolution Neural Network and Covariance Pooling Model for Mineral Mapping of Porphyry Copper Deposit Using PRISMA Hyperspectral Data

Sima Peyghambari, Yun Zhang, Hassan Heidarian, and Milad Sekandari

Abstract

Mapping distribution of alterations around porphyry copper deposits (PCDs) greatly affects mineral exploration. Diverse geological processes generate irregular alteration patterns with diverse spectral characteristics in mineral deposits. Applying remotely sensed hyperspectral images (HSIs) is an appealing technology for geologic surveyors to generate alteration maps. Conventional methods mainly use shallow spectral absorption features to discriminate minerals and cannot extract their important spectral information. Deep neural networks with nonlinear layers can evoke the deep spectral and spatial information of HSIs. Deep learning–based methods include fully connected neural networks, convolutional neural networks, and hybrid convolutional networks like mixed convolution neural network and covariance pooling (MCNN-CP) algorithms. However, each has its advantages and limitations. To significantly avoid losing important spectral features, we proposed a new method by fusing a one-dimensional convolutional neural network (1D-CNN) with MCNN-CP (1D-MCNN-CP), achieving an overall accuracy (97.44%) of mineral mapping from PRISMA HSIs. This research deduced that 1D-MCNN-CP improved performance and reduced misclassification errors among minerals sharing similar spectral features.

Introduction

The development of hyperspectral remote sensing technology, which can capture images with narrow and contiguous spectral channels, made significant progress in geological investigations and mineral exploration (Kruse 2004; Beiranvand Pour and Hashim 2014; Bedini 2017; Peyghambari and Zhang 2021). Different spaceborne and airborne hyperspectral sensors such as Hyperion, Hyperspectral Mapper (HyMap), Advanced Visible Infrared Imaging Spectrometer (AVIRIS), DLR Earth Sensing Imaging Spectrometer (DESIS), PRecursore IperSpettrale della Missione Applicativa (PRISMA), and the Environmental Mapping and Analysis Program (EnMAP) were used for lithological and mineral mapping (Kruse 2004; Bedini 2011; Agrawal *et al.* 2023; Tripathi and Garg 2023). Hyperspectral satellite images acquired by Hyperion pioneered spaceborne hyperspectral remote sensing for decades (Beiranvand Pour and Hashim 2014; Chakouri *et al.* 2020; Guo *et al.* 2021). However, due to the low signal-to-noise ratio (SNR) and global data availability of Hyperion data, new hyperspectral satellites (e.g., PRISMA, DESIS, and EnMAP) with better worldwide coverage and spectral features have been launched. Recently launched PRISMA satellite sensor acquires visible and near-infrared (VNIR) spectral bands with SNR of >200:1 and shortwave infrared (SWIR) spectral bands with 100:1 SNR, which are reasonable for geologic mapping (Mishra *et al.* 2022; Shebl *et al.* 2023).

Identification and mapping of hydrothermal alteration zones are critical in mineral exploration projects. Porphyry copper deposits (PCDs) typically show potassic, phyllic, argillic, propylitic, and gossan hydrothermal alteration zones (Lowell and Gumbert 1970). Each alteration zone has been identified with specified hydrothermal minerals. Phyllic and argillic zones are defined by hydroxyl-bearing minerals such as muscovite and kaolinite, respectively. At the same time, the propylitic zone is distinguished by chlorite, epidote, and magnesium, iron, and calcium carbonates. The gossan zone includes iron-bearing minerals such as jarosite, hematite, and goethite. Different alteration minerals such as muscovite, kaolinite, chlorite, calcite, and goethite have distinctive absorption features in the VNIR and SWIR (400 to 2500 nm) spectral region (Hunt 1977, 1979; Clark 1999). Regarding these distinctive absorption features, hyperspectral images are efficient tools to map hydrothermal alteration zones around various ore deposits (Sabins 1999; Beiranvand Pour and Hashim 2014; Zhang *et al.* 2016; Graham *et al.* 2018; Hu *et al.* 2019; Peyghambari and Zhang 2021).

There are different techniques for mapping hydrothermal minerals out of hyperspectral images (HSIs). Spectral matching methods measure the similarity between an unknown target spectrum and a known reference spectrum (van der Meer 2004). However, these methods have difficulties dealing with mixed spectra from remotely sensed HSIs. At the same time, subpixel techniques extract the targets' spectra and compute their relative abundance within a pixel. As a subpixel method, mixture-tuned matched filtering (MTMF) is broadly used for mapping hydrothermal minerals. However, subjective thresholding is a significant issue with subpixel mineral mapping from HSIs. Using remotely sensed imagery, traditional machine learning algorithms have recently been increasingly used in geologic mapping. Conventional machine learning algorithms, including random forest (RF), k-nearest neighbour (KNN), and support vector machine (SVM), are the most commonly used methods in geologic mapping (Karimzadeh and Tangestani 2021; Hajaj *et al.* 2023; Shebl *et al.* 2023). The traditional machine learning methods are robust in some HSI classification tasks, specifically land-cover discrimination. However, due to the nonlinear nature of geological materials (minerals), the importance of some deep spectral features, and the low SNR of hyperspectral data, traditional machine learning algorithms are not robust enough to map spectral variations of minerals.

Sima Peyghambari and Yun Zhang are with the Geodesy and Geomatic Engineering Department, University of New Brunswick.

Hassan Heidarian is with the British Columbia Geological Survey, Ministry of Energy, Mines and Low Carbon Innovation.

Milad Sekandari is with the Department of Mining Engineering, Shahid Bahonar University of Kerman.

Corresponding author: Sima Peyghambari (Speygham@unb.ca)

Contributed by Prasad S. Thenkabail, January 16, 2024 (sent for review February 20, 2024; reviewed by Itiya Aneece, Rongjun Qin).

Photogrammetric Engineering & Remote Sensing
Vol. 90, No. 8, August 2024, pp. 511–522.
0099-1112/22/511–522

doi: 10.14358/PERS.24-00006R2

Recently, deep learning frameworks, a subsection of machine learning methods, have been developed as a robust technique to deal with the nonlinear nature of different objects and extract their deep spectral features (Li *et al.* 2019). Fully connected neural networks (FCNNs) are basic deep learning methods that include only fully connected neural networks or dense layers. To feed the FCNN, the hyperspectral data cubes must be flattened, which leads to missing the spatial information in the classification processes. Convolutional neural networks (CNNs) are the typical deep learning structures used in HSI classification (Guo *et al.* 2019). Basically, CNNs can extract the hierarchical spatial and spectral information from HSI. The one-dimensional convolutional network (1D-CNN) introduced by Hu *et al.* (2015) uses spectral vectors as the input of the framework (Chen *et al.* 2016; Zhang, Zhang *et al.* 2016). Two-dimensional convolutional neural networks (2D-CNN) were proposed to consider the spatial features and contextual information from the adjacent pixels (Chen *et al.* 2016; Guo *et al.* 2019). The three-dimensional convolutional neural networks (3D-CNN) were introduced to learn spectral and spatial information simultaneously. However, they may suffer from overfitting and computational complexities (Chen *et al.* 2016). Increasing the number of 3D convolutional layers may degrade the classification accuracies.

According to the literature review, applying only 2D-CNN and 3D-CNN has disadvantages, such as missing the spectral band information and increasing model complexities. To overcome this issue, Zhong *et al.* (2018) proposed spectral–spatial residual networks (SSRNs). However, SSRNs may make redundant networks and increase the computational cost. Roy *et al.* (2020) introduced the HybridSN, which used 2D-CNN on top of the 3D-CNN to extract more spatial features. Zheng *et al.* (2021) developed a hybrid CNN framework that used mixed convolutions and covariance pooling named MCNN-CP to use the structural advantages of the 3D and 2D convolutions for discriminative learning information and fewer parameters. The covariance pooling layer is applied to reduce the misclassification errors. Although this hybrid method boosts the classification results, it may lose some essential spectral information.

Several researchers used CNNs for the spatial and spectral extraction convolutional networks for lithologic and mineral mappings from remotely sensed hyperspectral data. Clabaut *et al.* (2016) used a 2D-CNN structure to detect gossans in the Canadian Arctic. Ye *et al.* (2020) evaluated the performance of 3D-CNNs for lithologic mapping from GF-5 HSI. Liu *et al.* (2021) assessed the different 1D, 2D, and 3D CNNs on the thermal infrared HSI with the aim of lithologic mapping around ore deposits. Fu *et al.* (2021) used a stacked autoencoder (SAE), 1D-CNN, 2D-CNN, a spectral–spatial feature fusion model, and MCNN-CP to compare hydrothermal alteration mapping from GF-5 HIS. Zhang, Yi *et al.* (2022) implemented 1D-CNN and fused 1D- and 2D-CNNs for mineral mapping from the HSI data set.

Regarding the above considerations, this research proposes a new fused CNN model. It assesses its performance with some of the main deep learning algorithms to improve the hydrothermal alteration mapping around the worldwide well known Sarcheshmeh porphyry copper deposit. The deep learning models, including FCNN, 1D-CNN, 2D-CNN, 3D-CNN, MCNN, and fused 1D-MCNN-CP, were implemented on the PRISMA HSI to make comparisons. The results demonstrated that MCNN-CP and fused 1D-CNN with MCNN-CP considerably boost the classification performance against 1D-, 2D-, and 3D-CNNs. Specifically, the 1D-MCNN-CP, as a combination of 1D-, 2D-, and 3D-CNNs, can enhance the robustness of spectral–spatial deep learning extractors to classify HSI data sets in mineral mapping. This research updates the reliability of spectral–spatial deep feature extractors in mapping hydrothermal minerals.

Deep Learning–Based Classification Models

Deep learning models have gained massive popularity in scientific computing. They use artificial neural networks to perform classification on large data sets. The FCNNs, recurrent neural networks (RNNs), long short-term memory networks (LSTMs), autoencoders (AEs), and CNNs commonly use deep learning techniques in image processing (Alzubaidi *et al.* 2021). For classifying geological materials, existing deep learning classification models can be grouped into the following categories: FCNN, 1D-CNN, 2D-CNN, 3D-CNN, and hybrid models like MCNN-CP.

Fully Connected Neural Network (FCNN) Model

FCNNs comprise multiple layers of nodes or neurons in the input, hidden, and output layers. The FCNN model, or multi-layer perceptron (MLP), consists of dependent nonlinear functions, including a neuron that applies a linear transformation to the input vector through a weight matrix (Lei *et al.* 2021). Then, a nonlinear transformation using a nonlinear activation function is applied to the dot product of the input vector and a weight matrix. There are different activation functions: sigmoid, hyperbolic tangent (tanh), rectified linear unit (ReLu) , etc. Due to its simplicity and not being computationally expensive, the ReLu function is considered the activation function for each hidden layer of neurons. In multiclass classification problems, the SoftMax activation function is applied to the last output layer. As a basic deep learning neural network structure, the FCNN was used in this study to discriminate different alteration minerals in PRISMA data (Figure 1). This fully connected neural network sequence includes four dense layers of 128, 256, 256, and 64 neurons, respectively. The learning rate was left with a small default value of 0.0001, meaning it needed more training time (Wilson and Martinez 2001). The HSI cubes must be flattened as spectral vectors for the fully connected hidden layers. Therefore, it is likely that the essential spatial information of the input data could not be considered.

Convolutional Neural Network (CNN)

CNNs have been widely used for the classification of hyperspectral data. The CNN structure typically comprises three different layers, including convolution, pooling, and fully connected network layers. The convolution layer consists of different kernels that slide and convolve across the input data to conduct the convolution operation. They exploit different levels of features from the input data at various locations to generate feature maps. Low-level kernels can extract the simpler and more distinctive features, while high-level kernels integrate all the previously detected features. The output of the convolve layers will be passed through a nonlinear activation function and sent to the next

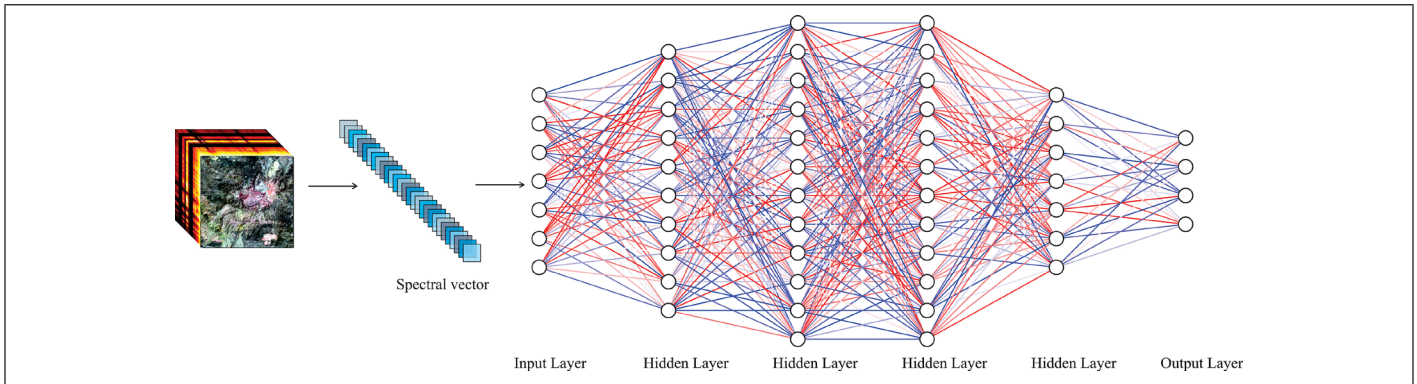

Figure 1. Fully connected neural network (FCNN) framework for remotely sensed hyperspectral image (HSI) classification.

layer. The pooling layers are used to downsample the spatial dimensions of the prior convolutional layer output. They decrease the required computation complexity and improve the translation invariance. Then, one or more fully connected (FC) layers are added to the preceding layers to generate the final output. They help to stack up the low-level information better and make final predictions (Hu *et al.* 2015; LeCun *et al.* 2015; Zhou *et al.* 2017). CNN models have fewer parameters than fully connected networks (FCNs), which can help mitigate overfitting. In deep networks, regularization techniques like dropout and batch normalization are typically integrated to enhance the model's ability to generalize to unseen or test data (Penatti *et al.* 2015). The dropout layer reduces the correlation between neurons by deactivating some neurons in the network, which provides more flexibility to the model (Tsagkatakis *et al.* 2019). Batch normalization is another technique to generalize the deep network, which normalizes the output of each layer to zero mean and unit variance to increase the model's initialization robustness and protect it from overfitting (Murugan and Durairaj 2017).

1D-CNN

Due to their high effectiveness in processing hierarchical data, various CNNs are increasingly used in HSI classification. The classification results of the 1D-CNN model have been used for comparison with other CNN architectures. Hu *et al.* (2015) modified the 1D-CNN model, consisting of two convolutional and two maximum pooling layers for the hyperspectral classification. They capture essential features of the input data and convert them into feature maps. The spectral vector of each pixel of the HSI was considered the input data. The fully connected layer operates on the feature maps and transforms them into feature vectors. The output of the fully connected layer is passed to the SoftMax function to create the final classification map (Figure 2). The 1D-CNN can capture spectral information; however, it ignores the important spatial information of the hyperspectral data.

The 2D-CNN and 3D-CNN architectures are currently used in most HSI classification problem models. Due to the computationally expensive nature of the 2D and 3D convolutional neural network frameworks and to reduce the spectral redundancy, the minimum noise fraction (MNF) transform was applied over the HSIs along the spectral bands. The result is transformed data into a new set of variables, including the same number of bands and spatial dimensions of the original HSIs. We selected the first 20 bands that contain and preserve the main spectral and spatial information of HSI. Assuming the HSI cube size is $H \times W \times D$, where W and H represent the width and height of the HIS, respectively, and D indicates the number of channels, the reduced MNF data cube has a size equal to $H \times W \times C$, where C is the channel dimension and $C \ll D$. Then, the MNF data are divided into small overlapping 3D cubes with a size equal to $w \times w \times C$, where w is the image cube width and height, and C is the number of MNF channels.

2D-CNN

2D-CNNs use 2D convolutional operations to scan across the input image using small kernels. The nonlinearity is then added to the convolved features by the activation function. In this research, we used (2,2) kernel size on the small 3D MNF cubes with the size of $7 \times 7 \times 20$ in 4 subsequent convolution layers. Only one maximum pooling layer is appended after the last convolution layer. Then, the output is flattened as the input vector of the fully connected layer (Figure 3). The activation function, SoftMax, is applied at the last layer to compute the probability of each class. Although 2D-CNN structures lead to preserving the important spatial features of the HSI, their 2D kernel type may result in ignoring significant spectral information of the HSI.

3D-CNN

The 3D-CNN framework uses the 3D kernel on the 3D data set to capture the spectral feature of the input data (Figure 4). In the 3D-CNN structure used in this study, we used $2 \times 2 \times 2$ kernels in the first

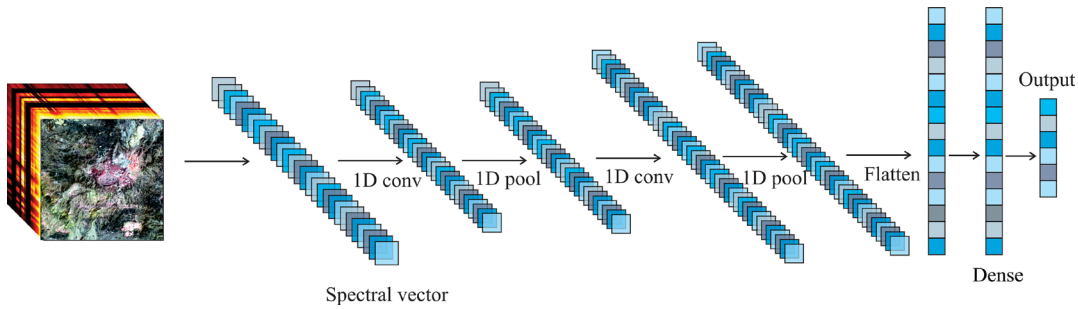

Figure 2. One-dimensional convolutional neural network (1D-CNN) framework for remotely sensed hyperspectral image (HSI) classification.

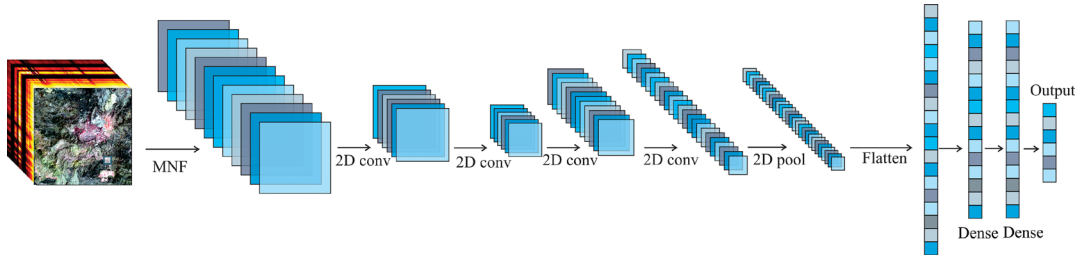

Figure 3. Two-dimensional convolutional neural network (2D-CNN) framework for remotely sensed hyperspectral image (HSI) classification.

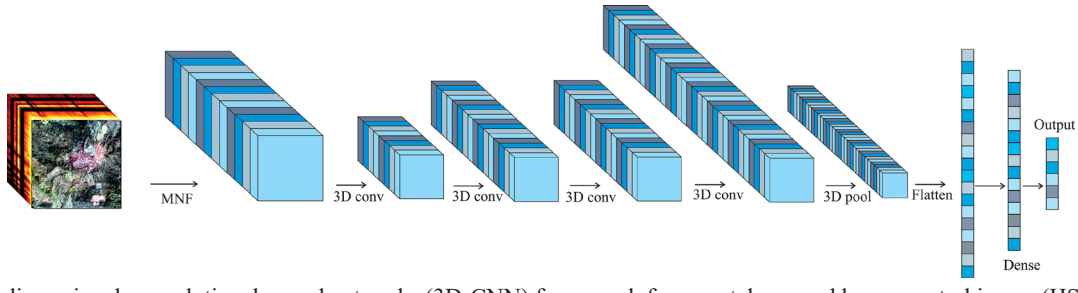

Figure 4. Three-dimensional convolutional neural networks (3D-CNN) framework for remotely sensed hyperspectral image (HSI) classification.

convolution layer and 3 × 3 × 3 kernels in the next three convolution layers over the 7 × 7 × 20 sized MNF data cubes to generate feature maps. The only maximum pooling layer is added to the last convolution layer. After flattening, the output is passed through the fully connected neural networks. The ReLu activation function was added to each layer to add nonlinearity to the model. The SoftMax classifier is then used at the last layer to create the final classification map.

Hybrid CNNs

Whereas the HSI classification task aims to capture the spectral information along with spatial information, 2D-CNN cannot handle the spectral information, and 3D-CNN can extract the spectral and spatial information with the cost of computational complexity. Therefore, various hybrid 2D and 3D CNNs were proposed, such as HybridSN (Roy *et al.* 2020) and MCNN-CP (Zheng *et al.* 2021). The HybridSN is three spectral–spatial 3D-CNN followed by a spatial 2D-CNN and fully connected layers. As proposed by Zheng *et al.* (2021), MCNN-CP used the same number of 3D- and 2D-CNNs to extract the fused spatial and spectral features, which are followed by reshaping the output tensor M to the matrix X. Then a covariance pooling was introduced to fully extract the second-order information from fused spectral and spatial features and reduce the hyperparameters for further processing (Figure 5). Although the MCNN-CP and other hybrid 2D- and 3D-CNNs can simultaneously deal with both spectral and spatial features of the HSI, they are still likely to lose the pixel-wise spectral information of the data. Their frameworks may affect adjacent pixels' spectra, which can affect the accuracy of classification results.

Proposed 1D-MCNN-CP Model

Based on the advantages and limitations of the aforementioned CNN models, we integrate MCNN-CP as the spectral–spatial feature extractor and 1D-CNN as the spectral feature extractor to propose a fused 1D-CNN and MCNN-CP model (named the 1D-MCMM-CP model), a two-branch feature fusion network, to use their complementary advantages and overcome their limitations. The spectral feature extractor aims to improve capturing the spectral features and the overall feature extraction process. It is worth mentioning that the spectral feature extractor was designed as 1D convolutional kernels over each pixel of the HSIs as the spectral vector. Using the 1D convolutional on the spectral vector makes the framework only focus on each pixel spectra during the spectral feature extraction (Figure 6). This process will reduce the involvement of spectrally unrelated information from adjacent pixels and enhance the classification performance. The contribution of adjacent pixel spectra has an unwanted spectral effect on each pixel spectrum, which is a frequent problem in geologic applications.

The extracted spectral–spatial features from the MCNN-CP were flattened and then fused with only the spectral features extracted from 1D convolutional and pooling layers. The two one-dimensional features are concatenated into a new one-dimensional vector with the total number of spectral–spatial and spectral features. Figure 6 shows a description of the proposed approach. It is worth mentioning that regularization techniques like dropout and batch normalization layers were added after each convolutional layer to increase the model's generalization capability. The shape of the 3D input for the spectral–spatial extractor was set as (7, 7, 20, 1), where 20 denotes the MNF subspace dimension, and the number of nodes in the output layer is set as 6, representing the number of classes in the data set. Random initialization is used to generate weights. Conducting a back-propagation algorithm, the model is trained using Adam optimizer by performing the SoftMax function. The batch size is 256, and the number of epochs is considered 100 for training the network.

Test Area, Data Source, and Ground Truth

Geological Setting of the Test Area

The test area is in the southeastern Uromiyeh-Dokhtar magmatic belt, Iran (Waterman and Hamilton 1975) (Figure 7a and 7b). This belt is an

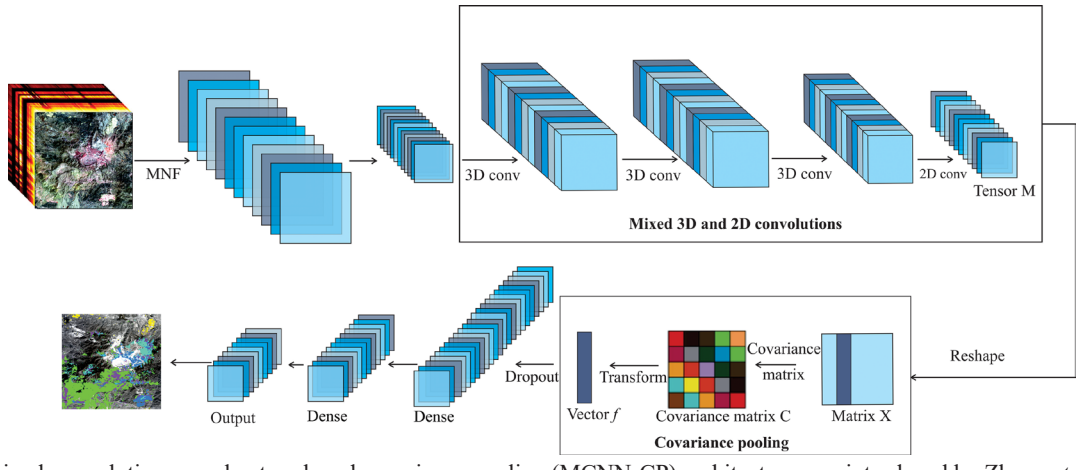

Figure 5. The mixed convolution neural network and covariance pooling (MCNN-CP) architecture was introduced by Zheng *et al.* (2021).

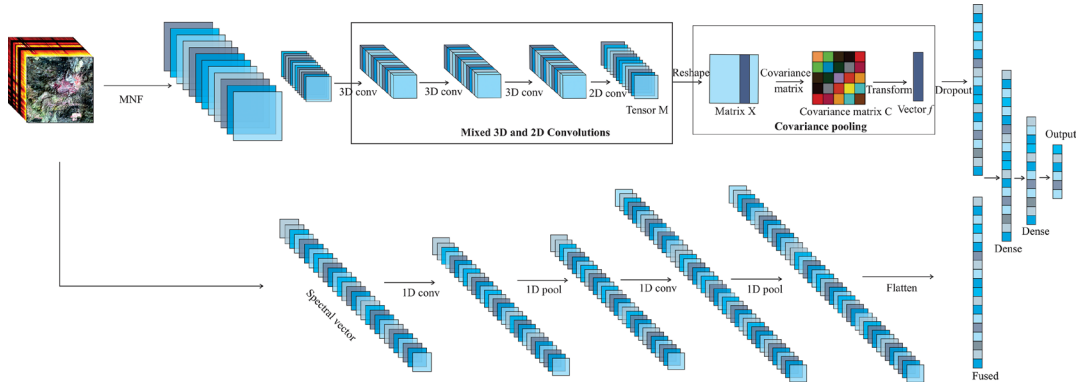

Figure 6. Proposed fused one-dimensional mixed convolution neural network and covariance pooling (1D-MCNN-CP) algorithm.

Alpine–Himalayan orogenic belt that extends from Europe to western Pakistan. Like other collisional magmatic arcs such as the North American Cordillera, the Andes, China, and Papua New Guinea, the Uromiyeh-Dokhtar magmatic belt hosted important PCDs. As the largest PCD in Iran, the Sarcheshmeh deposit is situated in the southeastern part of the Uromiyeh-Dokhtar magmatic arc. Hosted in a diorite to granodiorite stock, the Sarcheshmeh deposit has 1200 Mt copper and molybdenum (Waterman and Hamilton 1975; Aftabi and Atapour 2011). As a typical porphyry deposit, it has different hydrothermal alteration zones, including potassic, phyllic, argillic, and propylitic zones, respectively, from the inner to the marginal part of the deposit.

The Darrehzar porphyry deposit with 67 Mt copper is 8 km southeast of the Sarcheshmeh deposit. It has been hosted in the hydrothermally altered diorite and granodiorite rocks. The deposit shows similar alteration zones, including potassic, phyllic, argillic, and propylitic. Further supergene processes have formed reddish or yellowish gossan zones during extensive oxidation and sulfide leaching (Hosseinjani Zadeh *et al.* 2014). The propylitic zones surrounded the interior phyllic and argillic zones (Mijalkovic and Saric 1973). The sereidun deposit, located in the east proximity of the Sarcheshmeh deposit, includes phyllic, argillic, advanced argillic, and propylitic alteration zones. This alteration is followed by argillic and advanced argillic alteration zones (Barzegar 2007; Kazemi Mehrnia *et al.* 2011).

Data Set

The hyperspectral PRISMA pushbroom sensor was launched by the Italian Space Agency in March 2019 in a sun-synchronous orbit with 29 days revisiting time (Loizzo *et al.* 2019; Cogliati *et al.* 2021; Agenzia Spaziale Italiana 2022). Acquiring 238 spectral bands in 400 to 2500 nm (12-nm bandwidth), the PRISMA sensor has a 30-m spatial resolution. The PRISMA payload also contains a panchromatic (PAN) sensor, which captures the same area with a 5-m spatial resolution. The PRISMA images are acquired in interested areas ordered by the users, each covering a 30 × 30-km scene. The field investigations of altered minerals in the study area have been used to evaluate the accuracy of the results.

Generating Ground Truth Sample Data Set

To ensure a more reliable classification result, it is a key point to select and extract accurate features from the input data (Pal and Foody 2010). Thus, it is essential for supervised classifiers to select the best representative training and validating data. This research used several image-processing methods to identify and discriminate different minerals effectively. False color combination (FCC) of PRISMA bands (66-50-22 as RGB), as shown in Figure 8a, reasonably discriminated different alteration zones in the study area. MNF, a feature extraction technique, has been used to enhance the spectral contrast and discriminate different alteration zones within the area (Figure 8b). Developed by Green *et*

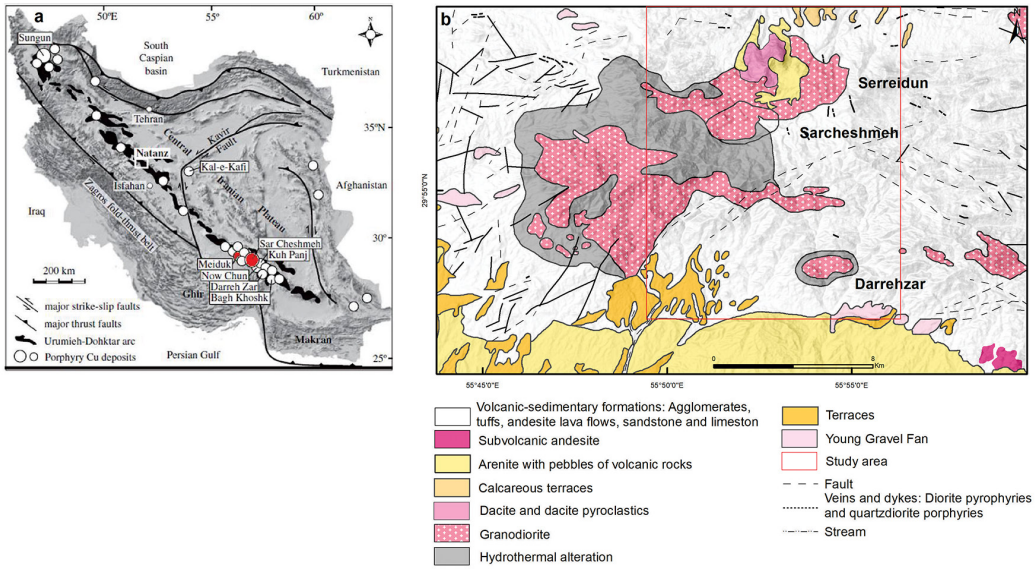

Figure 7. (a) Geological location of Sarcheshmeh deposit in Urumieh Dokhtar magmatic arc belt (Beiranvand Pour and Hashim 2011). (b) Geological map of Sarcheshmeh, Darrezar, and Sereidun porphyry copper deposit (modified after Dimitrijevic *et al.* 1971).

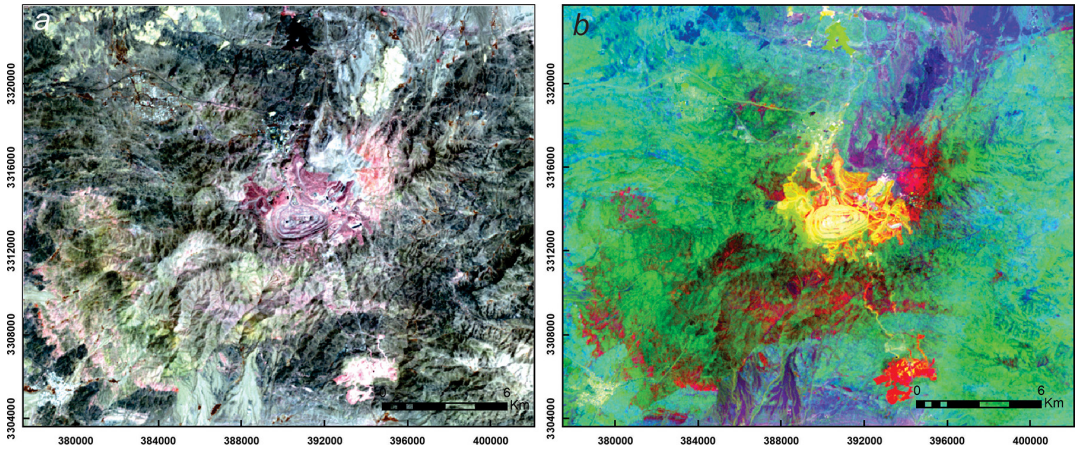

Figure 8. (a) False color combination (FCC) of PRISMA bands as RGB (B66-B50-B22). (b) Combination of first minimum noise fraction (MNF) bands to enhance the visual discrimination of different minerals.

al. (1988), the MNF transformation is an effective technique to reduce the inherent dimensionality of the hyperspectral data set and separate the random noise by transforming it into a series of images with a significant order. Combining the first MNF bands as RGB allows the grouping of similar pixels and effectively delineates the alteration zones. FCC and a combination of MNF bands could enhance the visual inspection of the HSI and confirm the geological fieldwork.

For supervised machine learning techniques and deep learning methods, it is necessary to have an appropriate sample data set to effectively analyze the data and extract and map the information to the output. A well labeled sample data set from distinct target minerals is required to analyze hyperspectral data to identify and discriminate different minerals. Supervised machine learning and especially deep learning algorithms need to have more training samples to perform better. However, the ground and hyperspectral data have a scale difference due to the low spatial resolution and ill-posed mixing problem in satellite-based hyperspectral remote sensing. Thus, the image spectrum is required to generate the sample ground truth data set.

In this research, we selected samples from certain regions of FCC and MNF band combinations. Fieldwork investigations obtained the location of sampled areas from the image. In the sample selection, we visually inspected the spectral curve and its absorption feature from all the pixels of the image. Five mineral types have been sampled from the PRISMA hyperspectral image from the Sarcheshmeh deposit and the surrounding area. The representative spectral feature of each mineral is shown in Figure 9. The spectral curves of the U.S. Geological Survey (USGS) library minerals have been added for comparison.

Muscovite, as a descriptive mineral of phyllic alteration, shows a distinct absorption at 2206 because of Al-OH vibration and a less intense absorption feature at 2240 and 2340 nm related to the presence of Al-OH molecules (Figure 9a) (Abrams *et al.* 1983). However, the abundance of iron oxide minerals causes an absorption at 930 nm in the muscovite spectral curve. Kaolinite, one of the descriptive clay minerals for argillic alteration, shows distinctive double absorption features at 2175 and 2206 nm due to the Al-OH vibration process (Figure 9b) (Clark 1999; Pontual *et al.* 2008). Because of iron and magnesium hydroxyls, chlorite, as the representative of the propylitic alteration zone, shows distinctive absorption features at 2250 and 2330 nm wavelength (Figure 9c) (Clark 1999). Calcite as a carbonate mineral exhibits an intense absorption feature at 2342 nm and less absorption at 2305 nm (Figure 9d). Iron oxides, another important group of minerals, were recognized from the PRISMA data. Because of charge transfer and crystal field, goethite and hematite have a diagnostic spectral absorption in the VNIR (Cudahy and Ramanaidou 1997; Zhang, Yi *et al.* 2016). Goethite (FeOx) shows an intense absorption at 930 nm and less absorption at 630 to 710 nm (Figure 9e) (Morris *et al.* 1985; Ducart *et al.* 2016). However, it also shows the 2206-nm absorption feature from the mixture with Al-OH minerals. Each mineral class was labeled as class 1 to 5. The average spectral features of each class are consistent with the USGS library spectra, representing the selected samples' reliability. A class labeled as the image background was added to the mineral class samples. The background samples were chosen from the pixels that do not overlap with the mineral samples and have spectrally different absorption features (Figure 9f). Table 1 shows the number of selected samples for this research. Figure 10 represents the distribution of ground truth samples used in this study.

Table 1. Sample data set of the test area.

Class No.	Category	Sample Pixel Count
Class 1	Goethite	1000
Class 2	Muscovite	1224
Class 3	Kaolinite	1010
Class 4	Chlorite	3274
Class 5	Calcite	1000
Class 6	Background	1324

Experiments

This research used the atmospherically corrected PRISMA (L2D level) of the study area. The absolute geolocation error of about 100 m of the L2D PRISMA was improved using the Landsat-8 multispectral data. Several preprocessing methods have been applied to the surface reflectance PRISMA data to ensure better results. The bad bands, including those covering water absorption features (B57 to B63, B69 to B73, B83 to B93, B105 to B121, and B149 to B179), were eliminated;

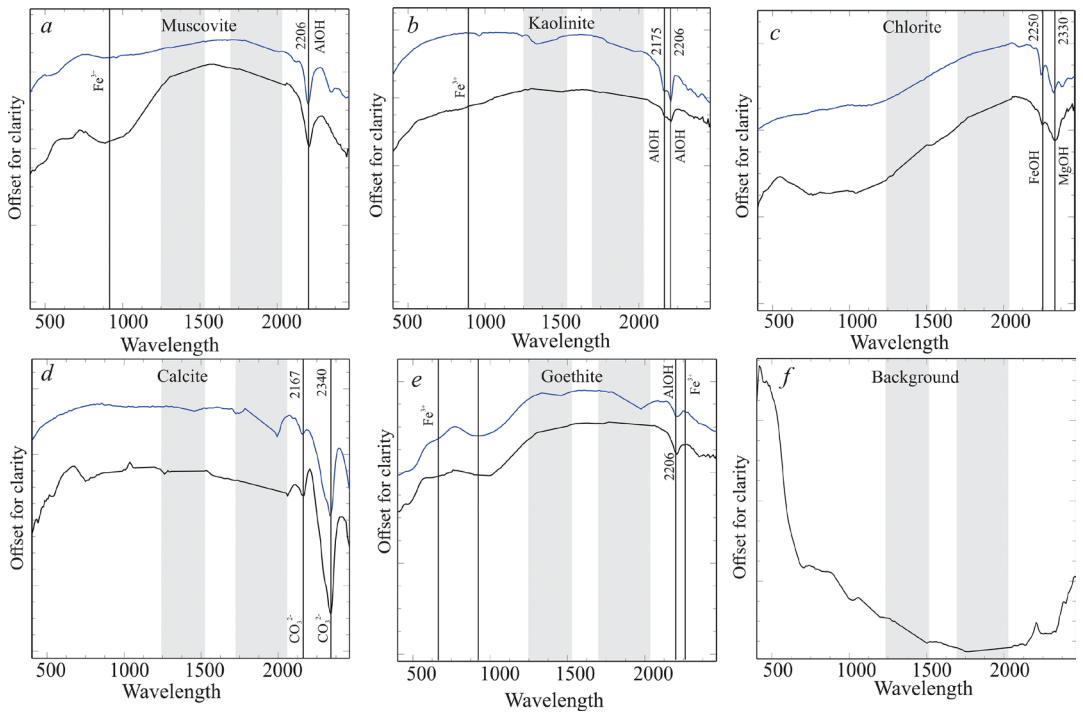

Figure 9. Mean PRISMA L2D spectrum of corresponding ground truth samples representative hydrothermal minerals, including muscovite (a), kaolinite (b), chlorite (c), calcite (d), goethite (e), and background (f) extracted from PRISMA imagery. The U.S. Geological Survey (USGS) spectrum (blue lines) is specified as blue for comparison.

only 156 of 238 primary bands were used for further processing. The PRISMA hyperspectral sensor suffers from smile properties, which cause distortions mostly in the VNIR spectrum wavelengths and can affect the accuracy of further classifications. The MNF method has been applied to reduce the smile effect on VNIR. To avoid the evaluation of the atmospheric components, the internal average relative (IAR) reflectance correction was used on the rest of the bands to normalize the image to a scene-average spectrum. The resulting spectral curve can be easily interpreted and compared with the USGS spectral library. These steps are performed using ENVI (5.6.3) software. The labeled data set was divided into training, test, and validation sets at 7:1.5:1.5. A total of 70% of the samples were used to train the model, and 15% were used as the validation set for the model performance evaluation. In addition, 15% of the samples were used as the test set, which was not used in training. They were used to evaluate the generalization capability of the model. Figure 11 represents the flowchart of the processing steps of our proposed 1D-MCNN-CP method, together with the processing steps of other existing CNN-based mineral classification methods (FCNN, 1D-CNN, 2D-CNN, 3D-CNN, and MCNN-CP). All the experiments are conducted under the same conditions using the same PRISMA data set for performance evaluation. The processing steps have been performed in Python 3.8.

Classification Results

Figure 12 displays the FCNN, 1D-CNN, 2D-CNN, 3D-CNN, MCNN-CP, and fused 1D-MCNN-CP classification maps. Table 2 represents the final training and validation accuracies of the six deep learning models. The training and validation accuracies of the six deep learning models are more than 90%. They are consistent with the overall accuracies, representing these models' good stability and generalization capability. To evaluate the accuracy of different methods, including the proposed approach, different evaluation measurements, such as average accuracy (AA), overall accuracy (OA), and kappa coefficient (Kappa) are used (Table 3).

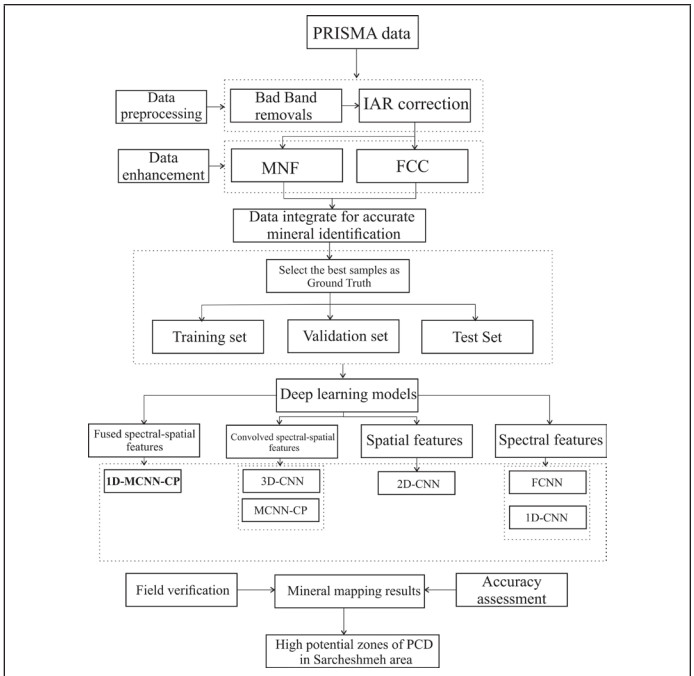

Figure 11. The processing steps of our proposed one-dimensional mixed convolution neural network and covariance pooling (1D-MCNN-CP) method and the fully connected neural network (FCNN), one-dimensional convolutional neural network (1D-CNN), two-dimensional (2D)-CNN), three-dimensional (3D)-CNN), and MCNN-CP methods were used in this study for mineral mapping from hyperspectral data.

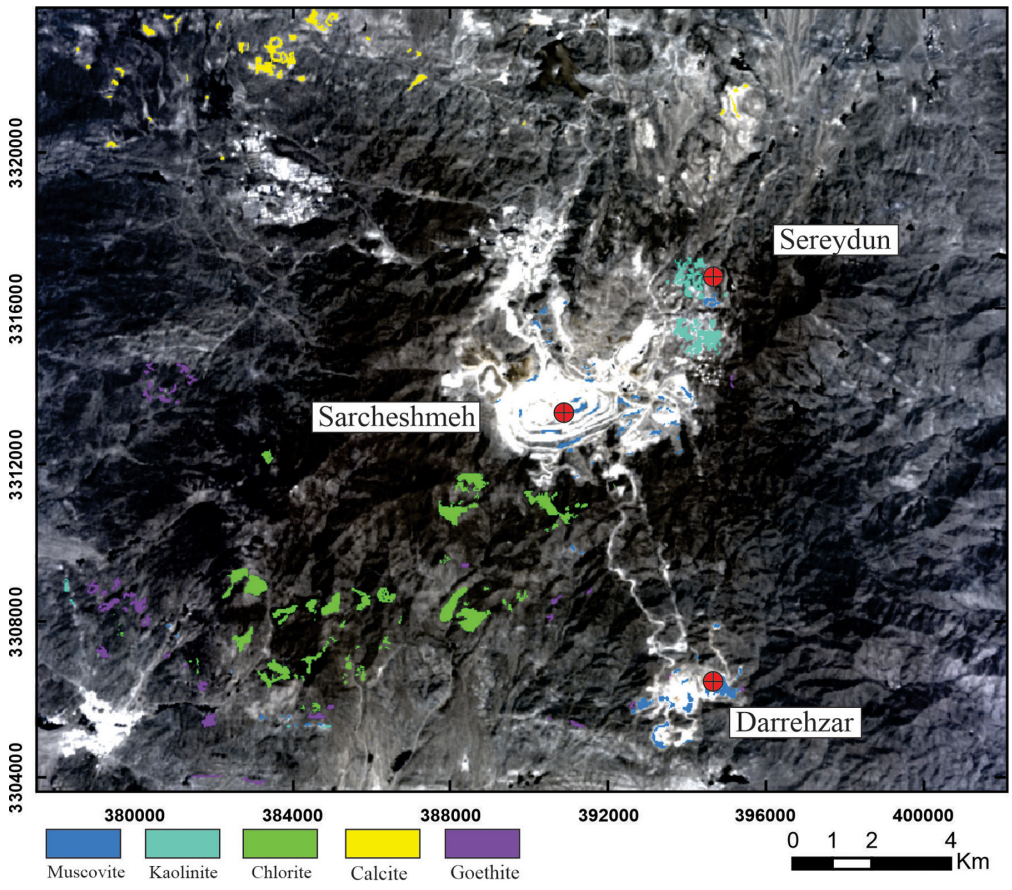

Figure 10. Distribution of ground truth samples in the Sarcheshmeh area.

Table 4 represents the F1 score of various classes over the different deep learning methods. The F1 score indicates the strength of classification models for different classes' performance. This implies that the model can efficiently discriminate positive cases by minimizing false positives and negatives. The confusion matrix represents the number of correctly predicted classes of classification models. Figure 13 shows the confusion matrix of different models performed in this study.

The results show that the spectral classifiers FCNN and 1D-CNN show the lowest OA accuracies, 91.49% and 91.94%, respectively. Regarding the F1 score (Table 4), they show weak performances in classifying goethite, muscovite, calcite, and background. According to confusion matrix outputs, the FCNN mostly misclassified goethite as chlorite and kaolinite as muscovite and goethite due to spectral similarities. It also shows the misclassification of calcite and background.

Table 2. Training and validation accuracies of the deep learning methods were used over the PRISMA data.

Method	Training Accuracy	Validation Accuracy
FCNN	91.48	91.57
1D-CNN	93.06	92.20
2D-CNN	91.77	92.65
3D-CNN	95.16	93.37
MCNN-CP	97.35	95.71
1D-MCNN-CP	98.76	96.73

1D = one-dimensional; 2D = two-dimensional; 3D = three-dimensional; CNN = convolutional neural network; FCNN = fully connected neural network; MCNN-CP = mixed convolution neural network and covariance pooling.

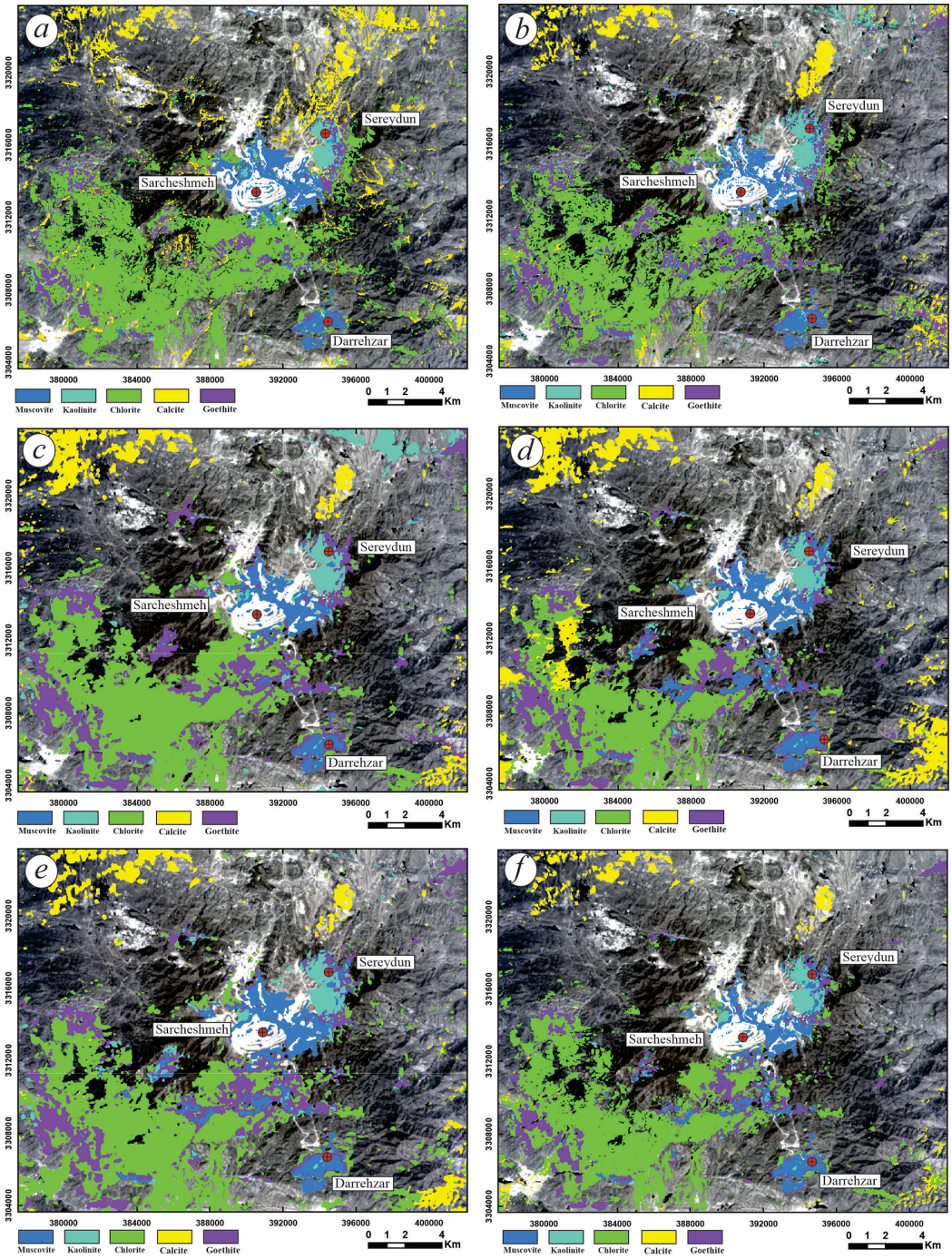

Figure 12. Classification results of fully connected neural network (FCNN) (a), one-dimensional convolutional neural network (1D-CNN) (b), two-dimensional (2D)-CNN (c), three-dimensional (3D)-CNN (d), mixed convolution neural network and covariance pooling (MCNN-CP) (e), and fused 1D-MCNN-CP (f).

Table 3. Classification results of deep learning methods were used over the PRISMA data.

Method	FCNN	1D-CNN	2D-CNN	3D-CNN	MCNN-CP	1D-MCNN-CP
Overall accuracy (%)	91.49	91.94	92.77	93.45	96.68	97.44
Average Accuracy (%)	91.23	91.32	92.84	93.89	94.97	97.30
Kappa × 100	89.76	90.25	91.30	92.13	94.11	96.91

1D = one-dimensional; 2D = two-dimensional; 3D = three-dimensional; CNN = convolutional neural network; FCNN = fully connected neural network; MCNN-CP = mixed convolution neural network and covariance pooling.

Table 4. F1 scores (%) measurements of different deep learning methods.

Method	FCNN	1D-CNN	2D-CNN	3D-CNN	MCNN-CP	1D-MCNN-CP
Goethite	81.27	91.22	88.78	93.17	92.09	96.24
Muscovite	96.14	91.40	90.14	93.46	90.15	96.76
Kaolinite	94.52	90.13	93.27	95.19	93.98	97.07
Chlorite	86.79	89.42	96.97	89.37	96.96	97.81
Calcite	93.95	95.83	93.74	98.56	99.05	98.06
Background	95.40	93.04	93.38	91.68	97.48	98.41

1D = one-dimensional; 2D = two-dimensional; 3D = three-dimensional; CNN = convolutional neural network; FCNN = fully connected neural network; MCNN-CP = mixed convolution neural network and covariance pooling.

The 1D-CNN spectral classification model misclassified goethite as muscovite, kaolinite, and chlorite; kaolinite as muscovite; and chlorite and calcite as background. The spatial 2D-CNN model shows an OA accuracy of 92.77%. It shows relatively better performance in terms of F1 scores than spectral models. However, based on the confusion matrix, it still suffers from misclassifying goethite as muscovite, kaolinite as muscovite, muscovite as goethite and kaolinite, and background as calcite. The spectral–spatial 3D-CNN obviously shows higher accuracy in terms of OA (93.45%) and better performance in terms of F1 score for different classes. The confusion matrix mostly misclassifies background as chlorite, muscovite as kaolinite, and goethite as muscovite. Integrating spectral and spatial features in MCNN-CP offered good classification accuracies regarding OA, AA, and Kappa (Table 3). Regarding the F1 score, the MCNN-CP also performs better than spectral and spatial models. According to the confusion matrix, it only suffers from the misclassification of muscovite as goethite and kaolinite and kaolinite as muscovite. The fused 1D-MCNN-CP shows the OA, AA, and Kappa accuracies as 97.44%, 97.30%, and 96.91%, respectively, with an improvement of around 1% compared to the MCNN-CP method. The remarkably higher F1 score of the fused approach compared to MCNN-CP indicates its best performance. It boosted the accuracy of muscovite and background with low misclassification errors. Although the MCNN-CP accurately discriminates most minerals based on F1 scores, the fused model performs better. Adding the 1D-CNN, fused the spectral feature of each pixel independently to avoid the effects of spectral features of adjacent pixels. The results of applied models indicated that adding pixel-wise spectral features to the spectral–spatial classifiers can learn more distinctive features and give better output mineral maps.

The classification maps of different alteration minerals around the Sarcheshmeh porphyry copper deposit were verified by field investigations (Figure 14). There is a reasonable correlation between the distribution of hydrothermal alteration minerals like muscovite and kaolinite in the classification outputs and their locations based on geological studies (Figure 14). According to Figure 14, sites 1, 2, and 3 represent phyllic, argillic, and gossan alterations, consistent with the classification mineral maps showing muscovite, kaolinite, and goethite, respectively. Sites 4 and 5 show phyllic and argillic alterations in the Darrehzar deposit and are consistent with the classification output. Site 6 in the Darrehzar deposit represents the aluminum, iron, and magnesium sulfate-bearing sediments correlated with iron-bearing gossan zones in the mineral map.

Figure 13. The confusion matrix of fully connected neural network (FCNN) (a), one-dimensional convolutional neural network (1D-CNN) (b), two-dimensional (2D)-CNN (c), three-dimensional (3D)-CNN (d), mixed convolution neural network and covariance pooling (MCNN-CP) (e), and fused 1D-MCNN-CP (f) models for the test data.

Ablation Study

The ablation study focused on the configurations of 1D-MCNN-CP on the same hyperspectral data presented in Table 5. For clarity in the evaluation, the model structures are segmented into four primary categories: 1D-MCNN-CP, MCNN-CP, 1D-3D-CNN, and 1D-2D-CNN. Notably, the 1D-MCNN-CP achieves better classification accuracy than the 1D-3D-CNN and 1D-2D-CNN.

Discussion

Experimenting with different deep learning algorithms to extract the spectral and spatial features of different hydrothermal alteration minerals from the PRISMA HSI data set reveals that the fusion of extracted spectral features with the spectral–spatial extracted features can promote the classification results. Conventional spectral mapping, such as band ratio and feature extraction methods like principal components analysis (PCA) and MNF, are not able to use valuable information from all the spectral bands of the HSI data set. These approaches can identify the discriminative spectral features. However, finding outcrops with distinct spectral absorption features in geological sites is not easy. The distinct geologic materials are mainly covered by weathered covering materials such as dust and lichen. The spectral matching methods can inspect the overall spectra; however, the noise might affect their performance. Also, they cannot distinguish the minerals with similar spectral features. On the other hand, subpixel techniques like MTMF methods have limitations with the subjective thresholding problem. Machine learning algorithms were introduced to help classify and map geologic materials. Although they consider all the spectral bands, they might have limitations in dealing with massive HSI data sets with complicated and different levels of spectral information.

In contrast with traditional methods, deep learning algorithms benefit from multi-layer frameworks with nonlinear functions to handle the HSI data set with a hierarchical structure. These architectures can simultaneously learn different levels of spectral and spatial information. Applying various types of deep learning in this study reveals that only spectral and spatial feature extraction methods such as FCNN, 1D-CNN, and 2D-CNN make identifying all the geological objects impossible. Integrating the spectral and spatial feature extractor layers can lead to discriminating minerals with similar spectral features and

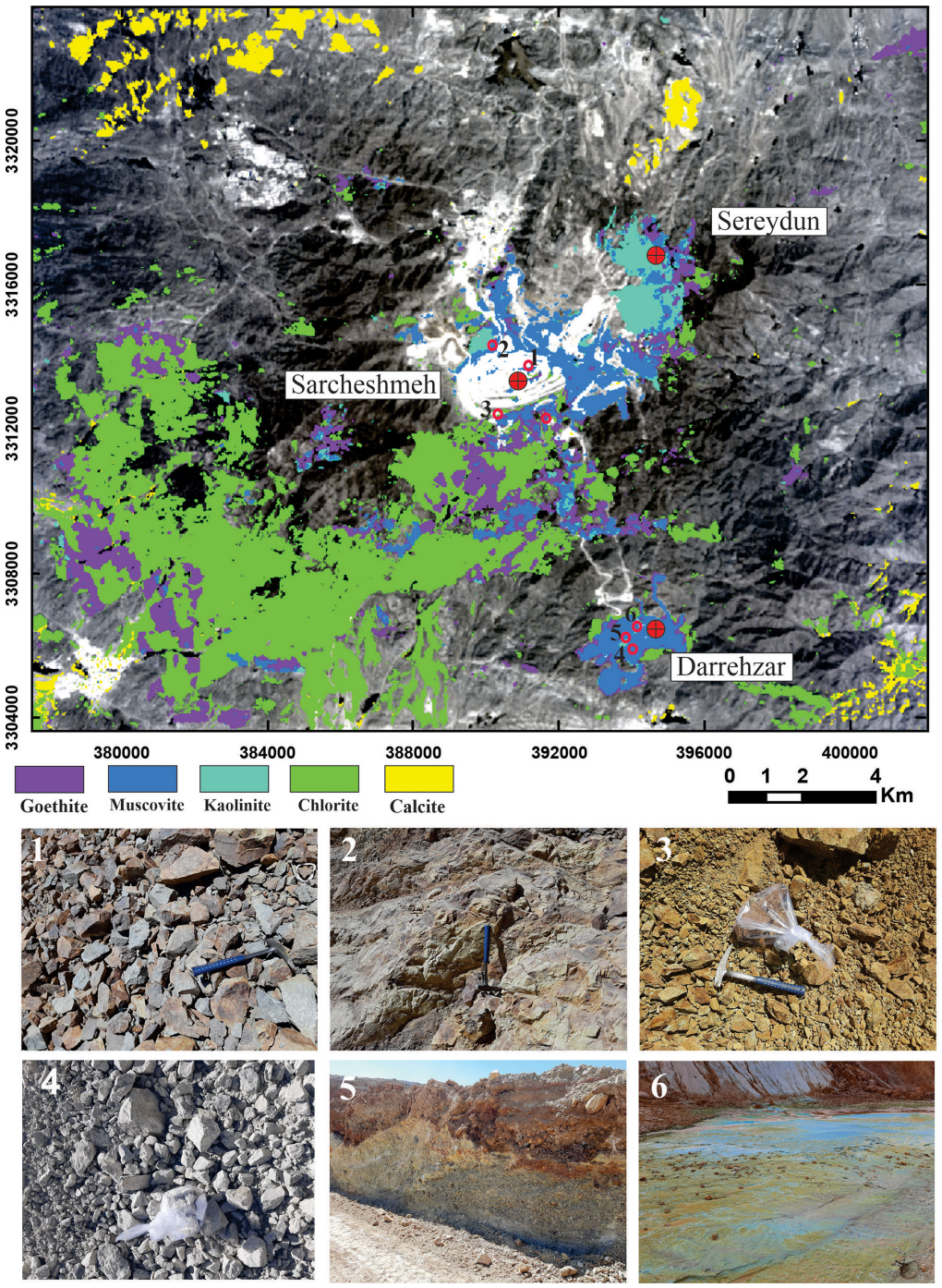

Figure 14. Field investigation results compared to those of the generated mineral maps.

Table 5. Ablation study results of 1D-MCNN-CP, MCNN-CP, 1D-3D-CNN, and 1D-2D-CNN configurations on the PRISMA data.

Method	1D-CNN[a]	2D-CNN[a]	3D-CNN[a]	Overall Accuracy	Average Accuracy	Kappa × 100
1D-MCNN-CP	✓	✓	✓	97.44	97.30	96.91
MCNN-CP	—	✓	✓	96.68	94.97	94.11
1D-3D-CNN	✓	—	✓	96.08	95.90	95.28
1D-2D-CNN	✓	✓	—	95.48	95.80	94.57

1D = one-dimensional; 2D = two-dimensional; 3D = three-dimensional; CNN = convolutional neural network; MCNN-CP = mixed convolution neural network and covariance pooling.
[a]The CNNs denoted by check marks are used in the corresponding models listed on the left. The dashes indicate the model was not used.

eliminating the salt and pepper noise from prior classification methods. Applying the 3D-CNN as the spectral–spatial extractor led to the mineral map having more accuracy in detecting distinct minerals and less scattered noises. However, there are some differences in discriminating backgrounds and minerals like calcite. Hybrid MCNN-CP shows improvement in terms of accuracy. However, it could not discriminate against some of the minerals. Adding the spectral extractor as 1D-CNN improves the detection of various minerals.

Accurately discriminating the hydrothermal alteration minerals, including goethite, muscovite, kaolinite, and chlorite, may generate the proper distribution of gossan, phyllic, argillic, and propylitic alteration zones, respectively, around the PCDs. According to the deep learning results in this research, 3D-CNN, MCNN-CP, and 1D-MCNN-CP show better performances, which might help predict areas with the potential for mineralization.

Conclusions

This research has aimed to use deep learning algorithms to extract the spectral and spatial features of different hydrothermal minerals and map them around the PCDs. The PRISMA HSI data set over the Sarcheshmeh porphyry copper deposit (southeastern Iran) was selected as the case study data. This geologic site is one of the well known PCDs around the world. Systematic preprocessing and processing steps have been applied to the HSI data set. Several deep learning frameworks have been constructed to extract the HSI data set's spectral, spatial, and spectral–spatial features.

Among the different models used, the spectral–spatial extractors achieved better accuracy. They benefit from the 1D-CNN and 2D-CNN models to delineate the HSI data's most useful spectral and spatial information. They also reduced the "salt and pepper" scatter noise and the misclassification of different minerals. Among these integrated methods, including 3D-CNN, MCNN-CP, and proposed fused 1D-MCNN-CP algorithms, the 1D-MCNN-CP approach shows the best performance in terms of OA (97.44%) due to its deep structure and adding pixel-wise spectral features. The results of the deep learning methods were validated via the field study samples and several previous field-based geologic maps around the studied area.

Acknowledgments

This study is supported by a research grant (to Yun Zhang) from the Canadian Space Agency's Flights and Fieldwork for the Advancement of Science and Technology Program. We appreciate the constructive comments provided by the editor and anonymous reviewers.

References

Abrams, M. J., D. Brown, L. Lepley and R. Sadowski. 1983. Remote sensing for porphyry copper deposits in southern Arizona. *Economic Geology* 78:591–604.

Aftabi, A. and H. Atapour. 2011. Alteration geochemistry of volcanic rocks around Sarcheshmeh porphyry copper deposit, Rafsanjan, Kerman, Iran: Implications for regional exploration. *Resource Geology* 61:76–90.

Agenzia Spaziale Italiana. 2022. PRISMA Products Specification Document, Issue 2.1.

Agrawal, N., H. Govil, G. Mishra, M. Gupta, and P. K. Srivastava. 2023. Evaluating the performance of PRISMA shortwave infrared imaging sensor for mapping hydrothermally altered and weathered minerals using the machine learning paradigm. *Remote Sensing* 15:3133.

Alzubaidi, L., J. Zhang, A. J. Humaidi, A. Al-Dujaili, Y. Duan, O. Al-Shamma, J. Santamaría, M. A. Fadhel, M. Al-Amidie and L. Farhan. 2021. Review of deep learning: Concepts, CNN architectures, challenges, applications, future directions. *Journal of Big Data* 8. https://doi.org/10.1186/s40537-021-00444-8

Barzegar, H. 2007. *Geology, Petrology and Geochemical Characteristics of Alteration Zones within the Seridune Prospect, Kerman, Iran*. Ph.D. dissertation, Aachen University, Aachen, Germany, 320 pp.

Bedini, E. 2011. Mineral mapping in the Kap Simpson complex, central East Greenland, using HyMap and ASTER remote sensing data. *Advances in Space Research* 47:60–73.

Bedini, E. 2017. The use of hyperspectral remote sensing for mineral exploration: A review. *Journal of Hyperspectral Remote Sensing* 7:189–211.

Beiranvand Pour, A. and M. Hashim. 2011. The Earth Observing-1 (EO-1) satellite data for geological mapping, southeastern segment of the Central Iranian Volcanic Belt, Iran. *International Journal of Physical Sciences* 6:7638–7650.

Beiranvand Pour, A. and M. Hashim. 2014. ASTER, ALI and Hyperion sensors data for lithological mapping and ore minerals exploration. *Springerplus* 3:130.

Boardman, J. W. and F. A. Kruse. 2011. Analysis of imaging spectrometer data using N-dimensional geometry and a mixture-tuned matched filtering approach. *IEEE Transactions on Geoscience and Remote Sensing* 49:4138–4152.

Chakouri, M., A. El Harti, R. Lhissou, J. El Hachimi and A. Jellouli. 2020. Geological and mineralogical mapping in Moroccan central Jebilet using multispectral and hyperspectral satellite data and machine learning. *International Journal of Advanced Trends in Computer Science and Engineering* 9:5772–5783.

Chen, Y., H. Jiang, C. Li, X. Jia and P. Ghamisi. 2016. Deep feature extraction and classification of hyperspectral images based on convolutional neural networks. *IEEE Transactions on Geoscience and Remote Sensing* 54:6232–6251. https://doi.org/10.1109/TGRS.2016.2584107.

Clabaut, É., M. Lemelin, M. Germain, M.-C. Williamson and É. Brassard. 2016. A deep learning approach to the detection of gossans in the Canadian Arctic. *Remote Sensing* 12:3123.

Clark, R. N. 1999. Spectroscopy of rocks and minerals and principles of spectroscopy. In *Manual of Remote Sensing*, *Volume 3: Remote Sensing for the Earth Sciences*, Hoboken, New Jersey: Wiley, pp. 3–58.

Cogliati, S., Sarti, F., Chiarantini, L., Cosi, M., Lorusso, R., Lopinto, E., Miglietta, F., Genesio, L., Guanter, L., Damm, A., Pérez-Lopez, S., Scheffler, D., Tagliabue, G., Panigada, C., Rascher, U., Dowling, T. P. F., Giardino, C, Colombo, R., 2021. The PRISMA imaging spectroscopy mission: overview and first performance analysis. *Remote Sensing for Environment* 262:112499.

Cudahy, T. J. and E. R. Ramanaidou. 1997. Measurement of the hematite: Goethite ratio using field visible and near-infrared reflectance spectrometry in channel iron deposits, Western Australia. *Australian Journal of Earth Sciences* 44:411–420.

Dimitrijevic, M. D., M. N. Dimitrijevic, M. Djordjevic and I. Djokovic. 1971. *Geological Survey of Iran* 1: 100,000 Series. Sheet 72, 50.

Ducart, D. F., A. M. Silva, C.L.B. Toledo and L. M. de Assis. 2016. Mapping iron oxides with *Landsat-8*/OLI and EO-1/Hyperion imagery from the Serra Norte iron deposits in the Carajás Mineral Province, Brazil. *Brazilian Journal of Geology* 46:331–349.

Fu, H., Q. Cheng, L. Jing and Y. Ge. 2021. Deep learning-based hydrothermal alteration mapping using *GaoFen-5* hyperspectral data in the Duolong Ore District, Western Tibet, China. *Journal of Applied Remote Sensing* 15:44512.

Graham, G. E., R. F. Kokaly, K. D. Kelley, T. M. Hoefen, M. R. Johnson and B. E. Hubbard. 2018. Application of imaging spectroscopy for mineral exploration in Alaska: A study over porphyry Cu deposits in the Eastern Alaska Range. *Economic Geology* 113:489–510. https://doi.org/10.5382/econgeo.2018.4559.

Green, A. A., M. Berman, P. Switzer and M. D. Craig. 1988. A transformation for ordering multispectral data in terms of image quality with implications for noise removal. *IEEE Transactions on Geoscience and Remote Sensing* 26:65–74.

Guo, Z., Y. Jiang and S. Bi. 2019. Detection probability for moving ground target of normal distribution using infrared satellite. *Optik* 181:63–70.

Guo, X., P. Li and J. Li. 2021. Lithological mapping using EO-1 Hyperion hyperspectral data and semisupervised self-learning method. *Journal of Applied Remote Sensing* 15:32209.

Hajaj, S., A. El Harti, A. Jellouli, A. B. Pour, S. Mnissar Himyari, A. Hamzaoui and M. Hashim. 2023. Evaluating the performance of machine learning and deep learning techniques to HyMap imagery for lithological mapping in a semi-arid Region: Case study from Western Anti-Atlas, Morocco. *Minerals* 13. https://doi.org/10.3390/min13060766.

Hosseinjani Zadeh, M., M. H. Tangestani, F. V. Roldan and I. Yusta. 2014. Sub-pixel mineral mapping of a porphyry copper belt using EO-1 Hyperion data. *Advances in Space Research* 53:440–451.

Hu, W., Y. Huang, L. Wei, F. Zhang and H. Li. 2015. Deep convolutional neural networks for hyperspectral image classification. *Journal of Sensors* 2015:1–12.

Hu, B., B. Wan, Y. Xu, L. Tao, X. Wu, Q. Qiu, Y. Wu and H. Deng. 2019. Mapping hydrothermally altered minerals with AST_07XT, AST_05 and Hyperion datasets using a voting-based extreme learning machine algorithm. *Ore Geology Reviews* 114:103116. https://doi.org/https://doi.org/10.1016/j.oregeorev.2019.103116.

Hunt, G. R. 1977. Spectral signatures of particulate minerals in the visible and near infrared. *Geophysics* 42:501–513.

Hunt, G. R. 1979. Near-infrared (1.3–2.4) μm spectra of alteration minerals—Potential for use in remote sensing. *Geophysics* 44:1974–1986.

Karimzadeh, S. and M. H. Tangestani. 2021. Evaluating the VNIR-SWIR datasets of WorldView-3 for lithological mapping of a metamorphic–igneous terrain using support vector machine algorithm: A case study of Central Iran. *Advances in Space Research* 68:2421–2440.

Kazemi Mehrnia, A., I. Rasa, S. Alirezaei, H. Asadi Harooni and J. Karami. 2011. Alteration mapping at Saridoon porphyry copper prospect using short wave infrared spectrometry (PIMA), ASTER satellite image and XRD. *Scientific Quarterly Journal of Geosciences* 20:3–12.

Kruse, F. A. 2004. Mineral mapping with AVIRIS and EO-1 Hyperion, in *Proceedings of the 12th JPL Airborne Earth Science Workshop*. Pasadena, California, 24–28 February 2003, 149-156.

LeCun, Y., Y. Bengio and G. Hinton. 2015. Deep learning. *Nature* 521:436–444.

Lei, X., Y. Fan, K. C. Li, A. Castiglione and Q. Hu. 2021. High-precision linearized interpretation for fully connected neural network. *Applied Soft Computing* 109:107572. https://doi.org/10.1016/j.asoc.2021.107572.

Li, S., W. Song, L. Fang, Y. Chen, P. Ghamisi and J. A. Benediktsson. 2019. Deep learning for hyperspectral image classification: An overview. *IEEE Transactions on Geoscience and Remote Sensing* 57:6690–6709. https://doi.org/10.1109/TGRS.2019.2907932.

Liu, H., K. Wu, H. Xu and Y. Xu. 2021. Lithology classification using TASI thermal infrared hyperspectral data with convolutional neural networks. *Remote Sensing* 13:3117. https://doi.org/10.3390/rs13163117.

Loizzo, R., M. Daraio, R. Guarini, F. Longo, R. Lorusso, L. Dini and E. Lopinto. 2019. Prisma mission status and perspective, in *IGARSS 2019-2019 IEEE International Geoscience and Remote Sensing Symposium*, Yokohama, Japan, July 28-Agust 2, 2019, 4503–4506.

Lowell, J. D. and J. M. Gumbert. 1970. Lateral and vertical alteration–mineralization zoning in porphyry ore deposits. *Economic Geology* 64:373-408.

Mijalkovic, N. and V. Saric. 1973. Exploration for ore deposits in Kerman region. Report No. YU/53, Geological Survey of Iran.

Mishra, G., H. Govil, A. Guha, H. Kumar, S. Kumar and S. Mukherjee. 2022. Comparative evaluation of airborne AVIRIS-NG and spaceborne PRISMA hyperspectral data in identification and mapping of altered/weathered minerals in Jahazpur, Rajasthan. *Advances in Space Research*. https://doi.org/10.1016/j.asr.2022.09.047.

Morris, R. V., H. Lauer, Jr., C. A. Lawson, E. K. Gibson, Jr., G. A. Nace, G. A. and C. Stewart. 1985. Spectral and other physicochemical properties of submicron powders of hematite (α-Fe_2O_3), maghemite (γ-Fe_2O_3), magnetite (Fe_3O_4), goethite (α-FeOOH) and lepidocrocite (γ-FeOOH). *Journal of Geophysical Research: Solid Earth* 90:3126–3144.

Murugan, P. and S. Durairaj. 2017. Regularization and optimization strategies in deep convolutional neural network. arXiv:1712.04711 [cs.CV]. https://doi.org/10.48550/arXiv.1712.04711.

Pal, M. and G. M. Foody. 2010. Feature selection for classification of hyperspectral data by SVM. *IEEE Transactions on Geoscience and Remote Sensing* 48. https://doi.org/10.1109/TGRS.2009.2039484.

Penatti, O.A.B., K. Nogueira and J. A. Dos Santos. 2015. Do deep features generalize from everyday objects to remote sensing and aerial scenes domains?, in *Proceedings of the IEEE Conference on Computer Vision and Pattern Recognition Workshops*, 7–12 June 2015, Boston, Massachusetts, pp. 44–51.

Peyghambari, S. and Y. Zhang. 2021. Hyperspectral remote sensing in lithological mapping, mineral exploration and environmental geology: An updated review. *Journal of Applied Remote Sensing* 15:31501.

Pontual, S., N. Merry and P. Gamson. 2008. *GMEX: Spectral Analysis Guides for Mineral Exploration, Volume 1: Spectral Interpretation Field Manual*. Victoria, Australia: Ausspec International.

Roy, S. K., G. Krishna, S. R. Dubey and B. B. Chaudhuri. 2020. HybridSN: Exploring 3-D–2-D CNN feature hierarchy for hyperspectral image classification. *IEEE Geoscience and Remote Sensing Letters* 17:277–281. https://doi.org/10.1109/LGRS.2019.2918719.

Sabins, F. F. 1999. Remote sensing for mineral exploration. *Ore Geology Reviews* 14:157–183. https://doi.org/https://doi.org/10.1016/S0169-1368(99)00007-4.

Shebl, A., D. Abriha, A. S. Fahil, H. A. El-Dokouny, A. A. Elrasheed and Á. Csámer. 2023. PRISMA hyperspectral data for lithological mapping in the Egyptian Eastern Desert: Evaluating the support vector machine, random forest and XG boost machine learning algorithms. *Ore Geology Reviews* 161:105652. https://doi.org/https://doi.org/10.1016/j.oregeorev.2023.105652.

Tripathi, P. and R. D. Garg. 2023. Potential of DESIS and PRISMA hyperspectral remote sensing data in rock classification and mineral identification: A case study for Banswara in Rajasthan, India. *Environmental Monitoring and Assessment* 195:575.

Tsagkatakis, G., A. Aidini, K. Fotiadou, M. Giannopoulos, A. Pentari and P. Tsakalides. 2019. Survey of deep-learning approaches for remote sensing observation enhancement. *Sensors* 19:3929.

van der Meer, F. 2004. Analysis of spectral absorption features in hyperspectral imagery. *International Journal of Applied Earth Observation and Geoinformation* 5:55–68. https://doi.org/https://doi.org/10.1016/j.jag.2003.09.001.

Waterman, G. C. and R. L. Hamilton. 1975. The Sar Cheshmeh porphyry copper deposit. *Economic Geology* 70:568–576.

Wilson, D. R. and T. R. Martinez. 2001. The need for small learning rates on large problems, in *Proceedings of the International Joint Conference on Neural Networks*, 15–19 July 2001, Washington, D.C. https://doi.org/10.1109/ijcnn.2001.939002.

Ye, B., S. Tian, Q. Cheng and Y. Ge. 2020. Application of lithological mapping based on advanced hyperspectral imager (AHSI) imagery onboard *Gaofen-5* (GF-5) satellite. *Remote Sensing* 12:3990.

Zhang, T., G. Yi, H. Li, Z. Wang, J. Tang, K. Zhong, Y. Li, Q. Wang and X. Bie. 2016. Integrating data of *ASTER* and *Landsat*-8 OLI (AO) for hydrothermal alteration mineral mapping in Duolong porphyry Cu–Au deposit, Tibetan Plateau, China. *Remote Sensing* 8:890.

Zhang, C., M. Yi, F. Ye, Q. Xu, X. Li and Q. Gan. 2022. Application and evaluation of deep neural networks for airborne hyperspectral remote sensing mineral mapping: A case study of the Baiyanghe uranium deposit in Northwestern Xinjiang, China. *Remote Sensing* 14:5122.

Zhang, L., L. Zhang and B. Du. 2016. Deep learning for remote sensing data: A technical tutorial on the state of the art. *IEEE Geoscience and Remote Sensing Magazine* 4:22–40. https://doi.org/10.1109/MGRS.2016.2540798.

Zheng, J., Y. Feng, C. Bai and J. Zhang. 2021. Hyperspectral image classification using mixed convolutions and covariance pooling. *IEEE Transactions on Geoscience and Remote Sensing* 59:522–534. https://doi.org/10.1109/TGRS.2020.2995575.

Zhong, Z., Li, J., Luo, Z., and Chapman, M., 2018, Spectral-spatial residual network for hyperspectral image classification: A 3-D deep learning framework. *IEEE Transactions on Geoscience and Remote Sensing* 56: 847-858. https://doi.org/10.1109/TGRS.2017.1755542.

Zhou, F.-Y., L.-P. Jin, and J. Dong. 2017. Review of convolutional neural network. *Journal of Computers* 40:1229–1251.

The layman's perspective on technical theory and practical applications of mapping and GIS

MAPPING MATTERS

YOUR QUESTIONS ANSWERED

by Qassim Abdullah, Ph.D., PLS, CP
Woolpert Vice President and Chief Scientist

- **Have you ever wondered about what can and can't be achieved with geospatial technologies and processes?**
- **Would you like to understand the geospatial industry in layman's terms?**
- **Have you been intimidated by formulas or equations in scientific journal articles and published reports?**
- **Do you have a challenging technical question that no one you know can answer?**

If you answered "YES" to any of these questions, then you need to read Dr. Qassim Abdullah's column, Mapping Matters.

In it, he answers all geospatial questions—no matter how challenging—and offers accessible solutions.

Send your questions to Mapping_Matters@asprs.org

To browse previous articles of Mapping Matters, visit http://www.asprs.org/Mapping-Matters.html

"Your mapping matters publications have helped us a lot in refining our knowledge on the world of Photogrammetry. I always admire what you are doing to the science of Photogrammetry. Thank You Very much! the world wants more of enthusiast scientists like you."

"I read through your comments and calculations twice. It is very clear understandable. I am Honored there are experienced professionals like you, willing to help fellow members and promote knowledge in the Geo-Spatial Sciences."

YOUR COMPANION TO SUCCESS

PUBLISHING OPEN-ACCESS IN *PE&RS* IS NOW EASIER!

ASPRS has changed the subscription model of our monthly journal, *PE&RS*. ASPRS is waiving open-access fees for primary authors from subscribing institutions. Additionally, primary authors who are Individual Members of ASPRS will be able to publish one open-access article per year at no cost and will receive a 50% discount on open-access fees for additional articles.

- **Open Access matters!** By providing unrestricted access to research we can advance the geospatial industry and provide research that is available to everyone.
- **Institutions and authors receive more recognition!** Giving permission to everyone to read, share, reuse the research without asking for permission, as long as the author is credited.
- **Reputation matters!** Known for its high standards, *PE&RS* is the industry leading peer-review journal. Adding open access increases authors' visibility and reputation for quality research.
- **Fostering the geospatial industry!** Open access allows for sharing without restriction. Research is freely available to everyone without an embargo period.

Under the previous subscription model, authors and institutions paid $1500 or more in open-access fees per article. This will represent a significant cost savings. Open-access publications benefit authors through greater visibility of their work and conformance with open science mandates of funding agencies.

Subscriptions asprs.org/subscribe
Membership asprs.org/membership

asprs THE IMAGING & GEOSPATIAL INFORMATION SOCIETY

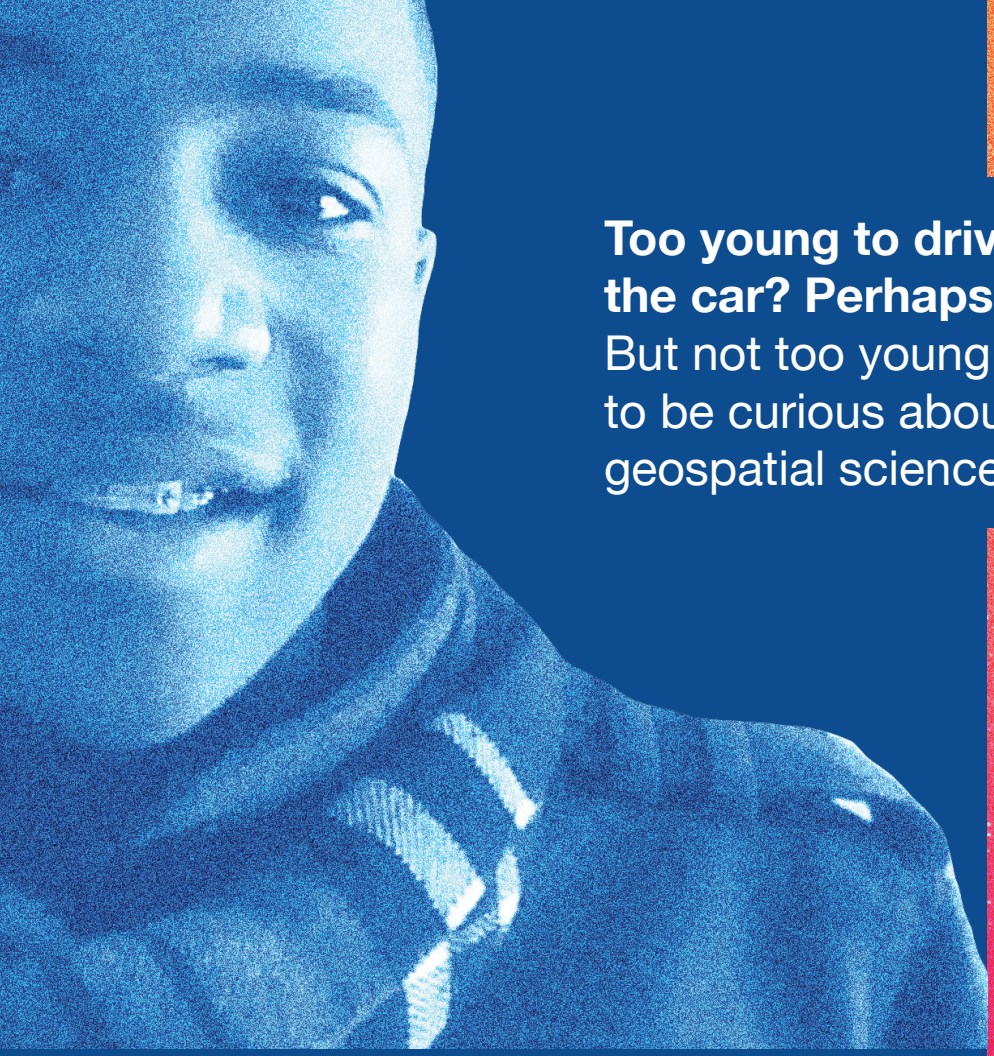

Too young to drive the car? Perhaps!
But not too young to be curious about geospatial sciences.

asprs FOUNDATION

The ASPRS Foundation was established to advance the understanding and use of spatial data for the betterment of humankind.

The Foundation provides grants, scholarships, loans and other forms of aid to individuals or organizations pursuing knowledge of imaging and geospatial information science and technology, and their applications across the scientific, governmental, and commercial sectors.

Support the foundation, so when they are ready, we are too.

asprsfoundation.org/donate

JOIN ASPRS TODAY!

asprs THE IMAGING & GEOSPATIAL INFORMATION SOCIETY

ACCELERATE YOUR CAREER!

PHOTOGRAMMETRY · REMOTE SENSING · GIS · LIDAR · UAS …and more!

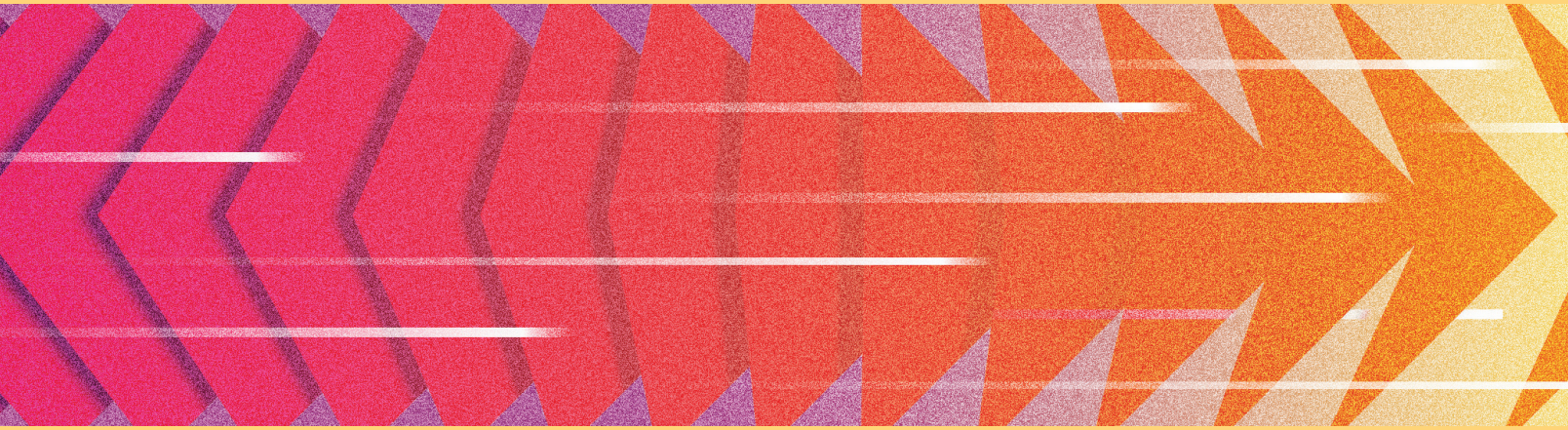

LEARN

- Read our journal, *PE&RS*
- Attend professional development workshops, GeoBytes, and online courses through the ASPRS ProLearn platform
- Earn professional development hours (PDH)
- Attend our national & regional meetings and conferences

DO

- Write for *PE&RS*
- Innovate to create new geospatial technologies
- Present at our national & regional meetings and conferences
- Engage & network

GIVE

- Participate in the development of standards & best practices
- Influence state licensure through our NCEES affiliation
- Mentor colleagues & support students
- Educate others about geospatial science & technology

BELONG

- Establish yourself as a geospatial expert
- Grow business relationships
- Brand yourself and your company as geospatial leaders
- Connect to the world via our affiliation with ISPRS

Don’t delay, join today at **asprs.org**